Master's Thesis

University of Zurich[UZH]

Photoconductivity in Superconducting $Bi_2Sr_2Ca_2Cu_3O_{10+x}$ Films

and

Effects of Electron and Neutron Irradiation on the Bose-Einstein Condensation in Magnetic Dimer Systems

Physik-Institut
Faculty of Science
University of Zurich

Daniel Destraz

June 2015

Under the supervision of Dr. A. Engel and Dr. H. Grundmann
in the group of Prof. Dr. A. Schilling.

Abstract

This master's thesis contains experiments in two different areas of solid state physics: the interaction of light with superconductors and the Bose-Einstein condensation in magnetic dimer systems. However, they do have one important aim in common: Trying to change, or better: increase, the temperature at which the corresponding phase transition occurs.

In the first part photoinduced conductivity in thin films of the material $Bi_2Sr_2Ca_2Cu_3O_{10+x}$ (BSCCO-2223) was examined. While photoconductivity has been mainly a topic of superconductor research during the 1990s, the explanation for the effect is still under some debate. The work done for this thesis was intended to shed some light onto these issues.

Different types of light sources, most of them lasers, were used and a wide range of wavelengths was covered. We found that our films of BSCCO show a photoinduced decrease in resistance in the range between 0.1% and 1%, which corresponds to a shift in T_c of a few mK. The minimum wavelength required for an effect to be observable is approximately 900 nm. However, there is no clear cut, instead the effect rather gets weaker and fades away for larger wavelengths. Intensity dependent measurements show a behaviour contradicting other published results and cannot be explained at this point. From temperature dependent measurements we concluded that the critical temperature plays an important role, as a different behaviour can be seen for lower and higher temperatures and the largest decrease in resistance upon illumination is observed at T_c. Measurements with X-ray photons show a much longer time scale of the decrease in resistance on the order of a day as compared to visible wavelengths for which the time scale is approximately one hour.

The occurrence of Bose-Einstein condensation in magnetic dimer systems has been the focus of intense research in recent years. This thesis focuses on the effect of disorder in such systems. The main research was done using $TlCuCl_3$, but samples of $Sr_3Cr_2O_8$ and $Ba_3Cr_2O_8$ were examined, too.

The irradiation of $TlCuCl_3$ with electrons did not result in any measurable effect of interest, however the irradiation with neutrons seems to have an effect that goes beyond simple uncertainties in the measurement.

Contents

Part I

Photoconductivity in Superconducting BSCCO Films

Chapter 1

Scientific Background

1.1 Overview

Photoconductivity in superconducting materials is an interesting phenomenon. It arises when light interacts with a superconductor in ways that lower its resistance. Two different kinds of photoconductivity can be distinguished: persistent photoconductivity and transient photocondutivity. In materials showing persistent photoconductivity, irradiation with light lowers the resistance to a level where it stays even after the light is turned off. Relaxation towards the original resistance only occurs at high temperatures.

It has been known for a long time that conventional superconductors react to light irradiation with an increase in resistivity, even destroying it completely in thin films [1].

After the discovery of high-T_c superconductors [2], these were quickly the target of similar investigations. In high-T_c superconductors in most cases the resistance decreases with illumination causing a shift of T_c to higher temperatures. This increased hopes in finding a room temperature superconductor, but to this day a T_c of $\approx 133\,\mathrm{K}$ (measured without any illumination) is still the maximum T_c ever found at ambient pressure [3].

1.2 Photoconductivity in High T_c Superconductors

1.2.1 Introduction

A vast number of different high-T_c superconductors has been investigated for their photoinduced resistance changes. The interest in this effect is in part due to the fact that a theory explaining high-T_c superconductivity is

still not in sight and results from such measurements might give an insight into the mechanism of high-T_c superconductivity. Another motivation to examine these materials are different types of applications, for example of the Josephson effect [4] or radiation detectors [5] that follow a similar mechanism as in superconducting nanowire single-photon detectors [6].

Oxygen deficiency is one important prerequisite for a high-T_c superconductor to exhibit photoconductivity. Fully oxygenated films, such as the material $Pr_yGd_{1-y}Ba_2Cu_3O_7$, show no sign of photoconductivity [7].

As in most other subfields of superconductivity, YBCO is one of the most extensively researched materials. Similar to low-T_c superconductors, light can increase the resistance of the cuprate $YBa_2Cu_3O_7$ thin films by breaking Cooper pairs. This is, however, only true for short time scales [8].

More interesting than an increase is a decrease in resistance. This has been shown to work exceptionally well for sufficiently large intensities [9]. Further investigations on $YBa_2Cu_3O_x$ show the doping dependence of the photoconductivity with a stronger relative decrease of resistance for lower x [10]. The authors of this publication report a shift of 5 K in T_c for $x = 6.55$. The same authors report an increased Hall coefficient, indicating a higher carrier concentration, as well as an increase in mobility of the carriers [11]. Even the transition from semiconducting to superconducting YBCO can be achieved by exposure to light [4]. The critical current density can also be enhanced, as shown by Dmitriev et al. [12].

An important feature in YBCO-123 is the presence of CuO chains. An example of a material without such chains is $Tl_2Ba_2CuO_{6+\delta}$. The effect measured here is very small, less than one percent for the resistance [13]. It is also interesting that either a decrease or an increase in resistance is observed in $Tl_2Ba_2CuO_{6+\delta}$ depending on wavelength.

1.2.2 BSCCO

The discovery of superconductivity in Bi-Sr-Ca-Cu-O, short BSCCO, was made in 1988 by Maeda et. al. [14]. The chemical formula for this material type is $Bi_2Sr_2Ca_{n-1}Cu_nO_{2n+4+x}$. The films used in our experiment were of the n=3 kind, so they have the chemical formula $Bi_2Sr_2Ca_2Cu_3O_{10+x}$, which was discovered by Tallon et. al. in 1988 [15]. The difference between the different materials of this type is the amount of CuO_2 planes in the structure.

One important difference in the structure of BSCCO and YBCO are the CuO chains. YBCO has chains of copper and oxygen next to the CuO_2 planes. BSCCO does not have any such chains.

Some research on BSCCO has already been conducted in the material $Bi_2Sr_2CaCu_2O_{8+\delta}$, however no photoconductivity has been observed [16].

The material $Bi_2Sr_2Ca_{1-x}Y_xCu_2O_{8+\delta}$ on the other hand does show the effect, albeit not the persistent kind, i.e. it relaxes back even at low temperatures.

1.3 Possible Explanations

The main structure that all cuprates have in common are CuO_2 planes separated by different kinds of interlayers. Some of the explanations for photoconductivity thus target those planes.

Measurements of the relaxation times have shown that they coincide with relaxation times for oxygen ordering [17]. Therefore, oxygen ordering has also been suggested as a possible explanation. In $GdBa_2Cu_3O_{6.3}$ photons with an energy of 4.1 eV lead to a particularly strong decrease in resistivity [18]. This energy corresponds to an electronic transition in a copper atom in the CuO chains with oxygen vacancies on both sides. The electron can get trapped in an oxygen vacancy and the hole can enter the valence band in the CuO_2 plane, which has a lower energy than the valence band of the CuO chains. Photons of lower energies can only excite electrons in the CuO_2 planes. The excited electrons as well as the holes created this way stay in the CuO_2 planes. This makes them more likely to recombine again. It has earlier already been suggested that the electron trapping is due to a local structural change that creates an energy barrier [19]. The model of electron trapping is also supported by the results showing stronger induced photoconductivity for lower oxygen content, i.e. more vacancies.

Experiments with X-rays in $YBa_2Cu_3O_6$ have shown photoconducting effects, too. The interpretation is that the X-ray photons induce damages in the material in the form of oxygen vacancies that act as traps for electrons [20]. Photoassisted oxygen ordering has been suggested to be the cause of photoconductivity by increasing the chain length and thereby increasing the doping [21]. A possible explanation for photoconductivity in materials without CuO chains is that electrons are trapped in other types of defects.

To summarize, most given explanations target the oxygen atoms in the chains in different ways, while their absence in form of an oxygen vacancy is usually emphasized.

Chapter 2

Experimental Setup

2.1 Cryogenics and Electronics

The BSCCO samples were attached to a copper sample holder with Silver Paint or Apiezon N. Silver paint turned out to be beneficial because it was more reliable in holding the sample in place over prolonged periods and provided a better thermal contact to the sample holder.

A Pt-100 thermometer was attached to the copper sample holder on the side opposite to the sample. This thermometer was used to control the heater by means of a PID controller. The precision of the temperature control was 1 mK for temperatures around 100 K.

The cryostat which was used for cooling the sample is capable of cooling down to $\sim 0.3\,\mathrm{K}$ with ^{3}He, however, the cooling was achieved with liquid nitrogen only, since for our material T_c ($\approx 105\,\mathrm{K}$) is well above 77 K. This was a simple way of saving costs on expensive helium and making the handling easier.

The vacuum shroud contains an exchangeable window, since different materials are transparent at different wavelengths of light. The heat shields inside the vacuum all have holes to achieve a direct unobstructed path from the light source outside to the sample inside.

The resistance was measured by the four point method. The dc current was kept constant by a Keithley current source. The voltage was measured with a nanovoltmeter. For each measurement point the current direction was reversed and the average resistance of the two directions was taken to reduce the effects of thermal electromotive forces.

2.2 Sample

The samples used in our experiments were made by Akiyoshi Matsumoto and Hitoshi Kitaguchi at the National Institute for Materials Science in Japan.

As described in ref. [22] the BSCCO films were grown on $SrTiO_3$ substrates by RF magnetron sputtering. The substrate temperature during the 2.5 h of sputtering was 620 °C and the pressure was 50 Pa of pure O_2. The target pellets for sputtering were made from oxide powders by means of heat treatment at 835 °C for 10 h and subsequent pressing and sintering at 840 °C for another 10 h. The targets then had a composition of $Bi_{1.5}Pb_{1.0}Sr_{2.0}Ca_{2.5}Cu_{3.0}O_x$.

After the sputtering, the samples were annealed at 840 °C for 100 h together with pellets composed of $Bi_{1.7}Pb_{0.3}Sr_{2.0}Ca_{2.0}Cu_{3.0}O_x$ in an atmosphere composed of O, Pb, and Bi. The post-annealing was done at 450 °C for 10 h in a pure oxygen atmosphere. The addition of a small amount of Pb improves the superconducting properties and stability of the material.

The sample thickness is $\approx$ 300 nm. Length and width are both $\approx$5 mm. The electrical contact was established by evaporating 2 nm of chromium and 50 nm of gold in four small stripes on the film, thermally annealing the sample at 400 °C in an O_2 atmosphere for 20 min, and subsequent bonding onto those stripes.

2.3 Light Sources

For this work multiple light sources were used. A red laser diode, three different fibre lasers, a quantum cascade laser, and an x-ray source. For the working principle of the laser diode and the x-ray source, which will be known to most of the readers, we refer to any introductory text book and/or the internet. The two more uncommon laser types, the fibre laser and the quantum cascade laser, are explained in the following.

2.3.1 Quantum Cascade Lasers

The first quantum cascade laser (QCL) was built at the Bell Laboratories in 1994 by J. Faist et al.[23]. These lasers are built out of quantum semiconductor structures, mainly InGaAs and InAlAs, by means of nanostructuring, such as MBE. Photons are emitted when electrons propagate trough multiple potential drops. Those steps in the potential can be seen as coupled quantum wells, hence the word 'quantum'.

The electronic states are strongly influenced by the quantum confinement perpendicular to the layers leading to discrete energy states. Parallel to the planes, however, they follow an almost parabolic shape. Unlike semiconductor lasers with bands of opposite curvature, QCLs have the bands curved in the same direction, making the energy distribution of the transition much narrower.

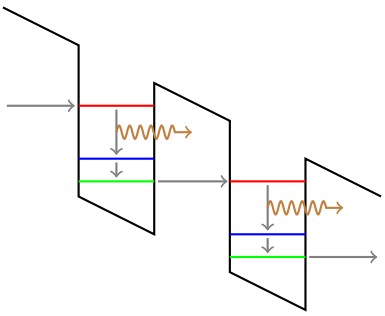

Figure 2.1: Simplified sketch of the energy levels in a quantum cascade laser. The potential is drawn in black, the path of the electron in grey. The electrons decay from the high energy state (red) into the lower energy state (blue) by emission of a photon (brown). By emitting a phonon the electrons decay into the lowest energy state (green), from which they tunnel to the high energy state of the next quantum well.

Electrical pumping to initiate population inversion is achieved by compositionally graded layers in between the active regions. The initial sawtooth shape of the potential wells changes to a staircase shape after an electric field of the order of $10^5\,\mathrm{V\,cm^{-1}}$ is applied. Electrons then enter the excited states in the wells by tunnelling from the graded regions. The tunnelling rate through this barrier is extremely fast, thus leading to a rapid filling of the excited state. While the laser is not yet lasing, the relaxation to the ground state happens very slowly. From the ground state the electrons tunnel, again relatively fast, into the next excited state in the well further down. In reality there is often an intermediate energy level in which the electrons fall by emission of a photon. From this level they then relax to the ground state before leaving this quantum well and entering the excited level of the next one. The energy of this last transition is tuned in such a way to ensure fast relaxation by means of phonons. Figure 2.1 shows the path of the electrons in the quantum well structure.

The slow relaxation time in comparison to the tunnelling time causes the population inversion necessary for lasers. During the laser operation, in the steady state, the rates of electrons entering the quantum well, the

rate of electrons undergoing stimulated decay, and the electrons leaving the quantum well is equal.

The QCL used for our experiments was able to emit radiation in the mid-infrared between 6 µm and 10 µm. The radiation was pulsed and the time between pulses could be set between 608 ns and 60.8 µs.

2.3.2 Fibre Lasers

Fibre lasers are a class of lasers that can achieve a very high bandwidth of wavelengths. The gain medium in these lasers is an optical fibre doped with rare earth elements [24]. In order to construct a laser resonator, the ends of the fibre need to be some kind of reflector. The pumping of fibre lasers is often done with laser diodes.

An important means to achieve the high bandwidth in these lasers is the so called supercontinuum generation by using nonlinear optics [25]. The medium which is used is a photonic crystal fibre. The light confinement here is achieved not by different materials with different refractive indices but by microstructured holes inside the fibre.

The rare earth dopants exhibit Stark splitting and are thus able to absorb and emit light with various wavelengths. These wavelengths then undergo a variety of processes such as Raman scattering, soliton dynamics, self-phase modulation, and four-wave mixing to broaden the spectrum until the supercontinuum is achieved [26].

To be able to conduct measurements with only one wavelength, so called acousto-optic tunable filters can be used [27, 28]. These filters have multiple channels per crystal and can be tuned to emit wavelengths within one octave. Two crystals were installed side by side in each of the two devices we received for testing. The two crystals cover two different wavelength regions, and, due to having two different exits, cannot be used simultaneously.

The working principle of acousto-optic tunable filters is based on acousto-optic diffraction in an optically anisotropic medium [29]. Acoustic waves, entering the crystal through a piezoelectric transducer driven by an electrical RF-signal, give rise to wavelength selective scattering by inducing variations in the refractive index of the crystal that act as a Bragg diffractor. An incoming light wave can, with the correct acoustic frequency, be reflected as a light wave orthogonally polarized to the initial one. The **k**-vector of the incident photon and the phonon then add up to the **k**-vector of the outgoing photon.

There were three different fibre lasers in use. Two were testing machines and the third one was the laser that was finally bought. One of the testing machines was from Fianium and the other one from NKT Photonics. The

laser from Fianium was found difficult to handle, both software- and hardware-wise. A big issue were back reflections into the laser during the beam alignment which caused its immediate shut down. The laser from NKT Photonics proved to be much more reliable and easier to use, which is one of the reasons why the decision was made to buy a laser from this company. However, no AOTF was bought and a grating monochromator was utilized.

One crystal of the AOTF of the Fianium laser was operating in the entire visible range. The second one, which was not used, in the infrared. The first crystal of the NKT laser was operating between 640 nm and 1100 nm. The second crystal at even longer wavelengths was not used either.

Chapter 3

Measurements

To make this chapter more understandable, a time line of the light sources and samples used will be given in the following. The first sample was used initially with the laser diode. Subsequently the Fianium fibre laser was used for a few measurements before switching to the quantum cascade laser. At this point the resistance of the sample had increased more than tenfold, which resulted in the replacement of the sample by a new one. This sample was then used for the rest of the measurements without showing a degrading like the first film experienced. All experiments were then performed with the rented NKT laser, except the temperature dependent measurements, which were done using the NKT laser that was bought by us. The last measurements performed were the x-ray measurements. In the following sections the results are grouped by light source instead of chronologically.

3.1 Resistance vs Temperature

The $R(T)$ measurement of the second film is shown in figure 3.1. A zoomed version can be seen in figure 3.2. If we take the center of the S-shaped part as the critical temperature, we find $T_\mathrm{c} = 105\,\mathrm{K}$. This is more clearly seen if one considers the derivative of the resistance with respect to the temperature. The maximum can be taken as a measure of T_c.

The second film had an equivalent curve, but due to the degradation of the film over time, the resistance increased gradually.

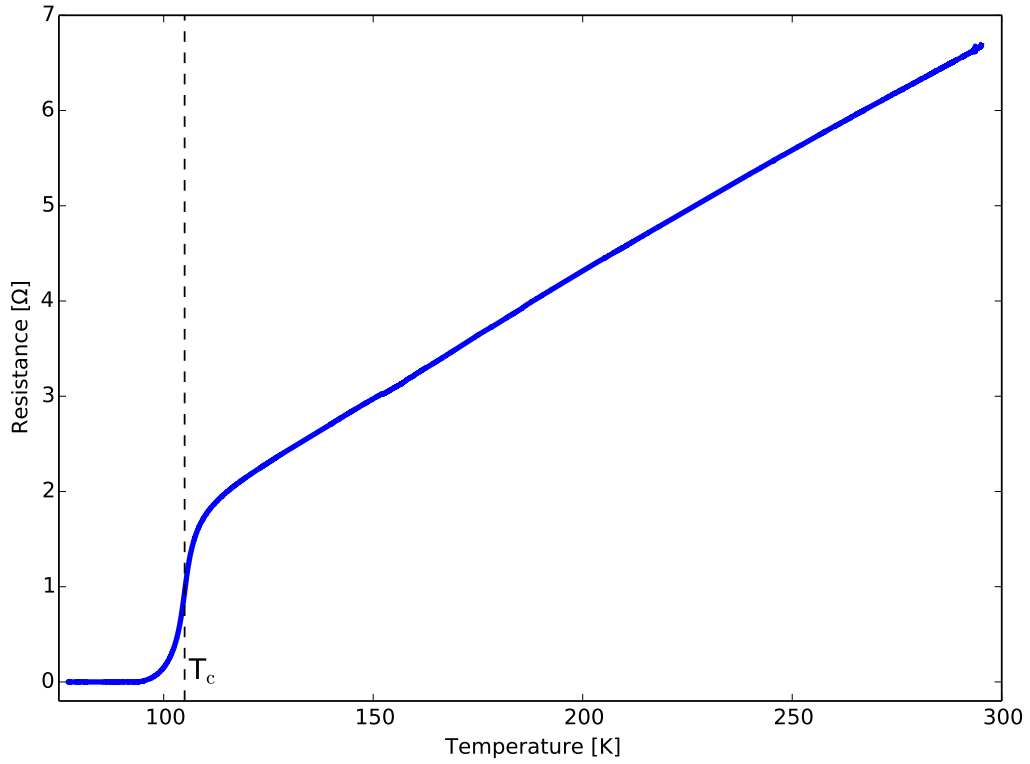

Figure 3.1: The $R(T)$-curve for the second film. It follows the expected shape with a linear decrease of R as T decreases down to temperatures close to T_c (black dashed line), where it falls off to $0\,\Omega$.

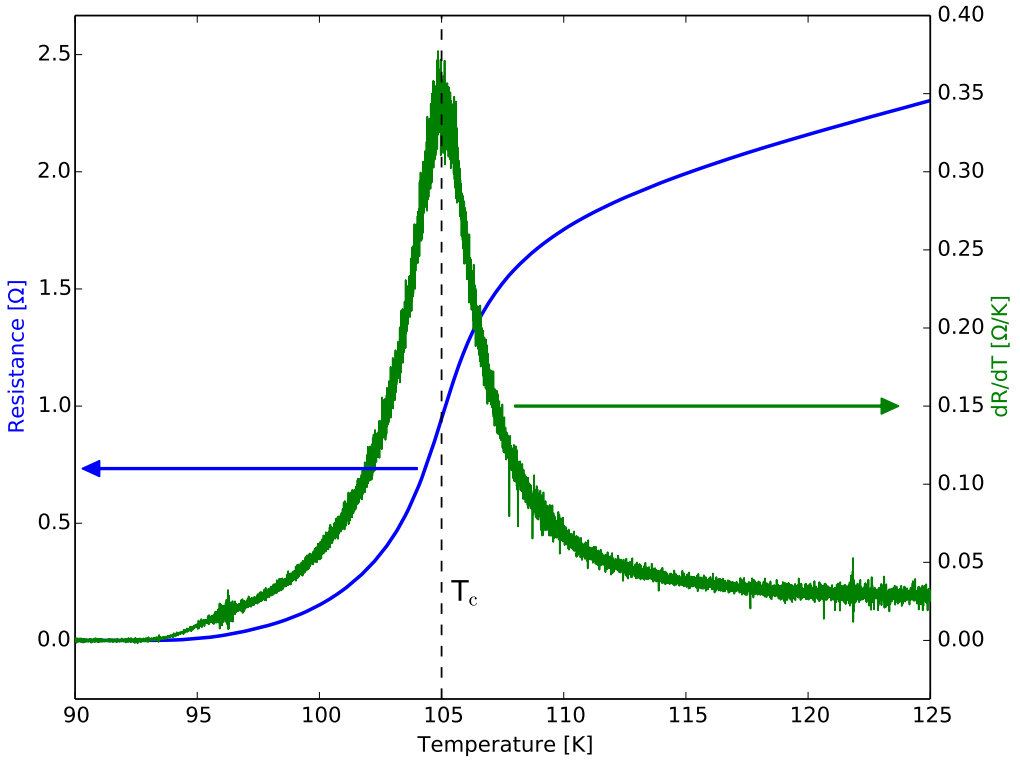

Figure 3.2: This graph shows in blue the same R(T) curve as figure 3.1 zoomed to the region around T_c. The green line shows the derivative, the black dashed line indicates T_c at 105 K

3.2 Laser Diode

A red laser diode was used to conduct tests with intensities on the order of a few mW/cm^2. A problem with this diode was the instability of the emitted intensity, which changed over time, especially in the short period after turning it on, where self-heating causes the temperature of the diode to increase, which has an influence on the diodes efficiency. To circumvent at least the initial, large change in intensity, a non-transparent object was placed in the beam instead of switching it off.

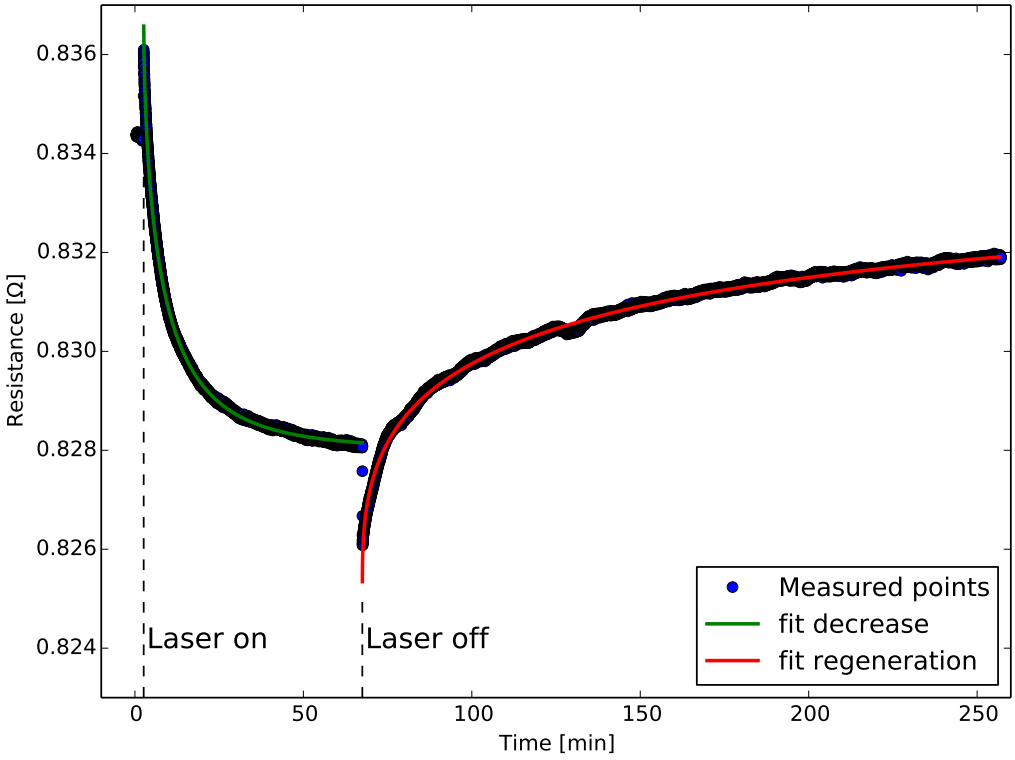

Figure 3.3: The change in resistance on illumination with red light at a temperature of 92.4 K. *The solid lines are fits according to function 3.1.*

In figure 3.3 such a measurement is shown. After switching the laser on a small jump occurs after which the resistance drops. When switching the light off a jump in the opposite direction occurs which is now followed by a regeneration towards the initial resistance. Both the decrease as well as the regeneration can be described by

$$R(t) = R_0 \exp\left(\left(\frac{t}{\tau}\right)^{\beta}\right) + R_\infty. \tag{3.1}$$

	R_j [mΩ]	R_0 [mΩ]	τ [min]	β	ΔR [mΩ]
during illumination	1.8(1)	8.54(1)	6.24(1)	0.624(1)	6.7(1)
after illumination	1.9(1)	8.33(3)	6.5(4)	0.411(1)	6.4(1)

Table 3.1: The values for the fitted functions from figure 3.3.

Equation 3.1 is a stretched exponential function, also known as the Kohlrausch function. One way to interpret this function is the occurrence of multiple independent exponential processes. In figure 3.3 the two solid lines are fits of the data to equation 3.1. Apart from a small overshoot at the start the data is described exceptionally well. This stretched exponential behaviour has been observed in almost all experiments on photoconductivity by any research group.

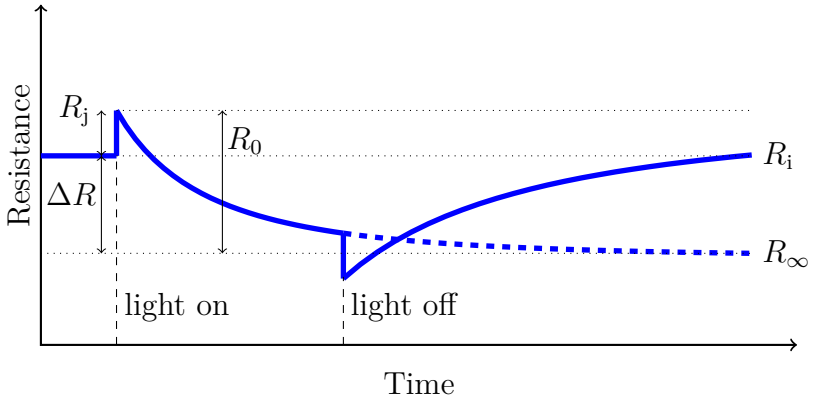

Figure 3.4: The explanation of the different values used to describe the R(t) measurements. R_i is the initial resistance before turning on the light. R_j is the jump height after turning on the laser. R_0 is the amplitude of the decaying resistance. R_∞ is the resistance that would be reached after an infinitely long irradiation. ΔR is the difference $R_i - R_\infty$. It is positive if $R_\infty < R_i$ and negative otherwise.

The parameters of the fitted functions in figure 3.3 are shown in table 3.1, their meaning is explained in figure 3.4. The values during and after illumination are roughly the same except for β which leads to the regeneration being more elongated than the decrease.

3.3 Quantum Cascade Laser

Further Experiments were performed with a quantum cascade laser. This laser sets itself apart from other systems by emitting radiation in the mid-infrared between 6 µm and 10 µm. To let radiation of these wavelengths pass into the cryostat, the window was replaced by a germanium window, which is non-transparent to visible light but transparent to longer wavelengths.

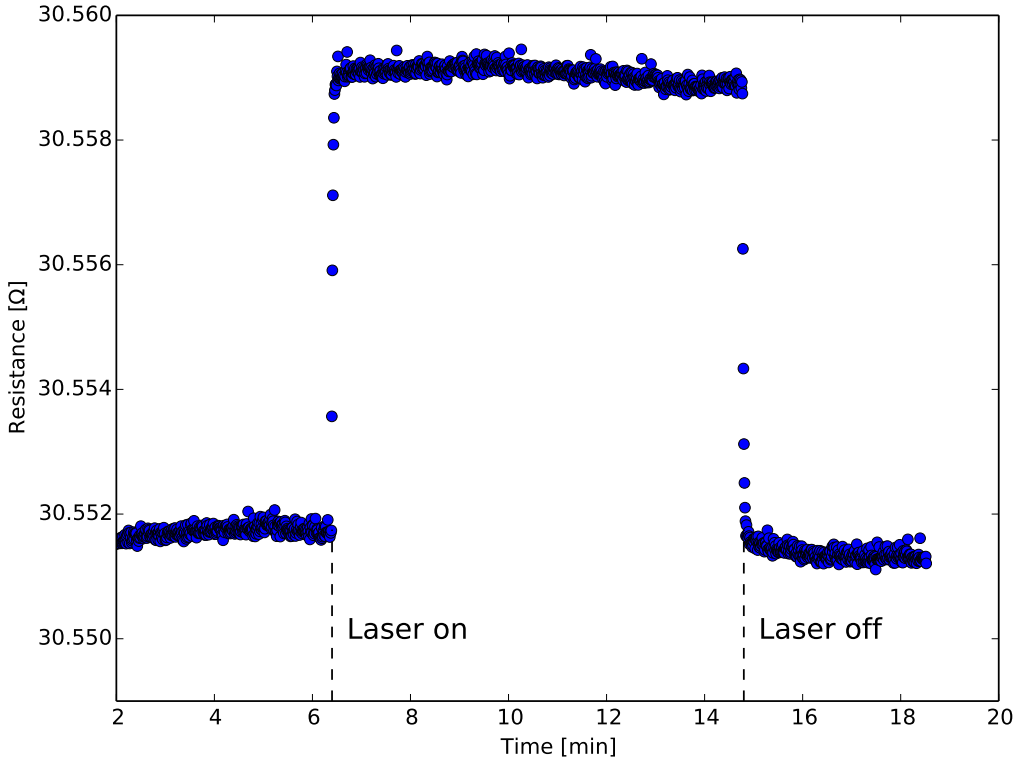

Figure 3.5: A measurement with the quantum cascade laser. This measurement was performed with $\lambda = 6.9\,\mu\text{m}$ and $T = 103\,\text{K}$. A jump in the resistance occurs when switching on the laser. Continued irradiation seems to have no effect on the resistance. When switching the laser off, the resistance drops back to the original value.

We conducted measurements with different intensities and wavelengths. Figure 3.5 shows a measurement with $\lambda = 6.9\,\mu\text{m}$, $T = 103\,\text{K}$, and a period of pulses every 6.08 µs, which corresponds to a repetition rate of the pulses of 164 kHz. Further measurements were done at the same wavelength but with pulses every 608 ns and every 60.8 ns.

No photoconductivity could be observed in any of the measurements with the quantum cascade laser. The jumps appearing when the laser is turned on or off are consistent with a simple heating of the film, as deduced from the linear dependence of the jump height on the power of the laser. Besides these jumps, no other influence of the laser could be detected.

The intensity is not known since the photodiodes that were available do not work at such long wavelengths. There are more reasons to why the light intensity on the sample was difficult to estimate. First, the different shieldings were not aligned perfectly, making only a smaller part of the film visible and only with a slight angle with respect to the normal of the window, which made it hard to adjust. Second a laser beam of such high wavelengths is invisible to the naked eye and to infrared cameras as well. Third, the window where the beam enters the cryostat was made of germanium, which is nontransparent to the human eye. For all these reasons it was unknown which part of the film was illuminated and what the ratio of unilluminated to illuminated area was.

One should also notice the high resistance in figure 3.5. For this laser we had to exchange the window and thus heat the sample to room temperature and afterwards cool it again. This process must have had a strong negative effect on the film and caused this increase in resistance. The film was replaced with a new one afterwards.

3.4 Fibre Lasers

The lowest wavelength for which a measurement with laser light was performed was 488 nm, which is in the blue region. For this the optical crystal of the AOTF for the Fianium laser was used. Figure 3.6 shows this measurement. The points in time when the laser was turned on and off can be seen easily due to the spikes in the resistance.

Measurements were also performed with green and red light and they both show the photoconductivity too. The laser then had to be sent back, as the testing period was limited. It helped us, however, to confirm the occurrence of photoconductivity up to the blue wavelength region.

We then progressed with the test laser from NKT photonics. One issue here was that the AOTF could only emit light with wavelengths down to 640 nm. The repetition rate of the first NKT laser was 78 MHz. With an additional option it would have been possible to choose other repetition rates. However, this option was not installed in the test device we received. The second laser we received had this option installed.

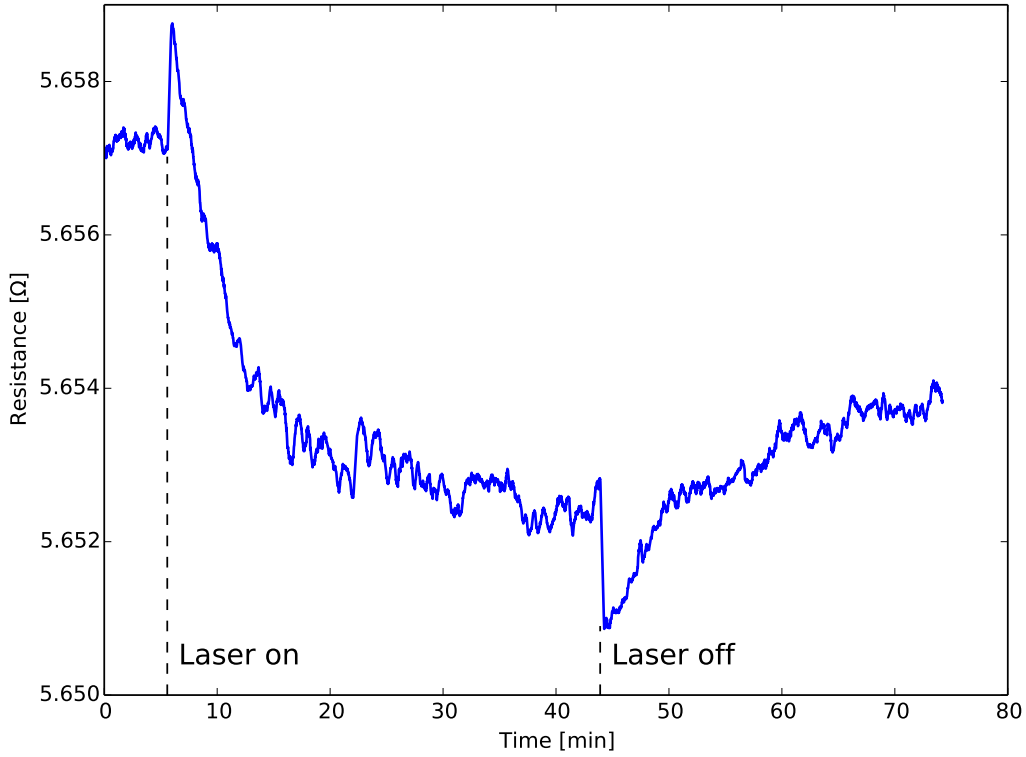

Figure 3.6: Here a measurement with $\lambda = 488\,\mathrm{nm}$ *and* $T = 103\,\mathrm{K}$ *is shown. The beginning of the irradiation after about* $5\,\mathrm{min}$ *and the end after* $44\,\mathrm{min}$ *can clearly be seen based on the jumps. Due to a small signal to noise ratio, the data was smoothed over 31 points by a running average.*

For the measurements with this laser, the sample was exchanged due to the large increase in resistance. After removing the old sample it was noticed that the film and the surrounding areas on the sample holder were covered with a greyish deposit. We did not find out what caused these problems and they did not occur again with the new film.

This laser was used to measure the dependence of the photoinduced effects on the intensity of the light. The temperature was chosen in such a way that the position on the $R(T)$-curve is around T_c. For these measurements the temperature was fixed at $105\,\mathrm{K}$ and the wavelength was set to $650\,\mathrm{nm}$. This particular wavelength was chosen for multiple reasons: First, red light is visible to the eye and one can thus visually confirm the operation of the laser. Second, the effect was found to work at least down to blue light and up to $\approx 900\,\mathrm{nm}$, making red a reasonable choice in the middle. Third, the AOTF crystal could operate for wavelengths as low as $640\,\mathrm{nm}$, so with $650\,\mathrm{nm}$

one is not yet right at the edge of the possible wavelength range. This would prevent a possible decrease in intensity and other negative effects that could occur at the very limit of wavelengths that the AOTF could transmit.

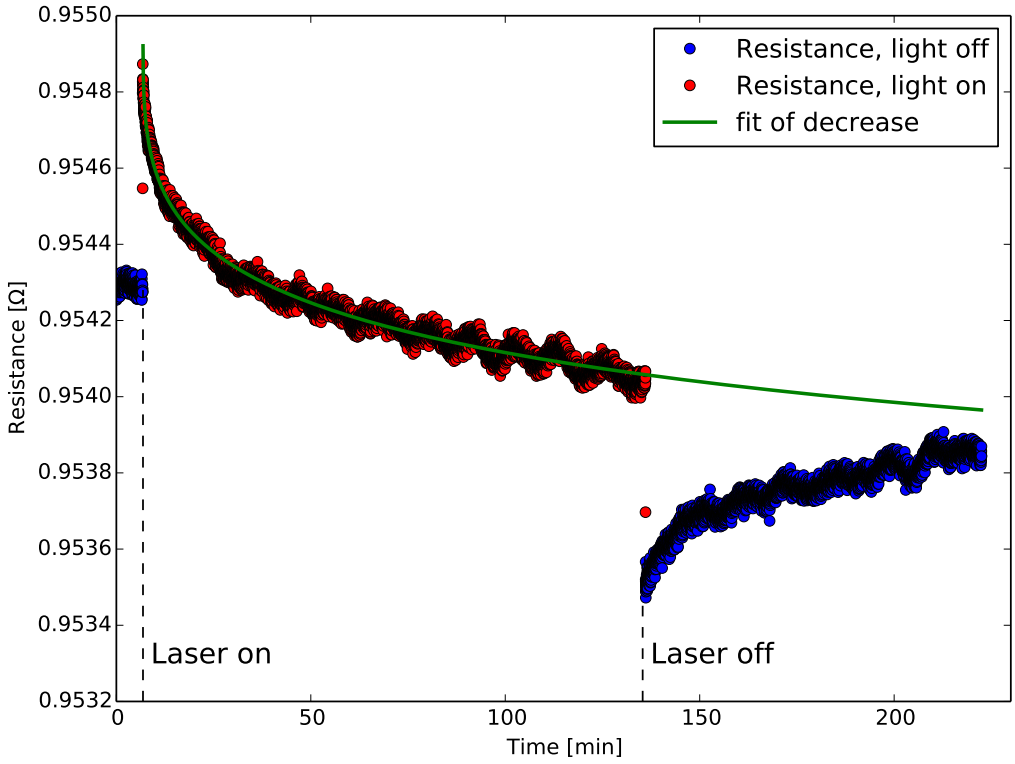

Figure 3.7: The R(t) curve including its fit according to equation 3.1 for $\lambda = 650\,\mathrm{nm}$ *with a power of* $65\,\mu\mathrm{W}$*. The part of the green line extending beyond the red points indicates the predicted continuation of the red points had the laser been left on.*

An example of a measurement with this laser is shown in figure 3.7. The function 3.1 used to perform the fits agrees to the data very well. There is also almost no overshoot right at the beginning.

The dependence on intensity is shown in table 3.2. The spot size of the laser is not known precisely, hence the power is given as it was measured with a photodiode. We estimated the spot size to be approximately $1\,\mathrm{mm}^2$. Some of the measurements did not run as expected and many problems occurred, such as temperature instabilities and jumps in resistance. The measurements shown, however, did run in an acceptable way. The setpoint is the power level that one can adjust in the laser control software and it corresponds to the output intensity, though it does not scale linearly, i.e. 20% is not half the

Setpoint [%]	Power [μW]	R_j [mΩ]	R_0 [mΩ]	τ [min]	β	ΔR [mΩ]
25	9.87	0.064(5)	0.150(5)	4.7(2)	0.71(4)	0.086(2)
26	15.9	0.118(9)	0.415(7)	62(2)	0.55(1)	0.293(5)
27	22.7	0.20(2)	2.3(5)	$\sim 2 \times 10^3$	0.35(1)	2.1(5)
29	41.5	0.22(2)	0.64(2)	42(3)	0.5(1)	0.42(1)
30	51.7	0.43(2)	0.58(2)	7.5(5)	0.24(2)	0.15(3)
31	65.6	0.72(8)	1.61(6)	$2.2(3) \times 10^2$	0.307(7)	0.89(5)
32	85.2	0.70(1)	0.69(1)	8.4(2)	0.500(9)	$-0.01031(5)$
33	105	0.9(1)	0.69(2)	12.5(3)	0.287(7)	$-0.151(7)$
34	128	1.1(1)	1.383(9)	9.8(2)	0.263(1)	$-0.1222(8)$
35	156	1.4(1)	3.5(5)	$\sim 5 \times 10^4$	0.13(1)	2.1(5)
36	192	1.6(1)	3(2)	$\sim 1 \times 10^4$	0.23(3)	?

Table 3.2: The values for measurements with different powers at $T = 105\,\mathrm{K}$ and $\lambda = 650\,\mathrm{nm}$. Entries marked with $\sim$ have errors that are as large or even larger than the value itself. The entry marked by a '?' is not known due to a bad shape of the curve and a large error on R_0. The last four entries for R_j are taken manually from the plots, the other entries are calculated from R_0 and ΔR. Positive values for ΔR indicate a decrease in resistance, negative values an increase.

power of 40%. Furthermore a setpoint of 20% for one wavelength is not necessarily the same power as a setpoint of 20% for another wavelength. This made the operation of the laser somewhat tedious.

The meaning of the different variables used to describe the time-dependent resistance are visualized in figure 3.4. The first important thing to notice is the absence of a measurement with a setpoint of 28%. The reason is that the $R(t)$ curve one gets from this measurement does not agree well with the function used to do the fits. The fit did only work with a very small range of starting parameters and the results depended strongly on small changes of the starting parameters. For example the time constant τ was, according to the fit, $\sim 10^{10}\,\mathrm{s}$. This is a strong discrepancy to the values of τ for other intensities. At first we had the assumption that the measurement had a problem and it was thus repeated, however, the fit did not work any better. Visually the $R(t)$-curves for this intensity do not look different from the other measurements. For now, without any further investigations, it appears to be an inexplicable behaviour. It might be the case that function 3.1 is not the optimal way of describing the data or that the parameters in the fit procedure should have been constrained to lower values.

A more understandable behaviour can be seen in R_j, which increases with increasing power. This is in agreement with the interpretation of the jump as a temperature rise since a higher power of the irradiation leads to a higher temperature. The jump height depends linearly on the power of the emitted light, as it should.

For R_0 the behaviour is again more unpredictable, but a notably large value exists for 27%. Only for very high powers such a value is found again. The reason for this large R_0 at 27% is not known, but it is reproducible. There might be a connection to the behaviour at 28%. Another issue at this power level is the weakening of the relaxation. It seems like the original value would not quite be reached again. The parameter R_0 is in a sense an extrapolation of how far the resistance would drop after an infinite amount of time. It is thus larger of what can be observed in the experiment on a time scale of one hour.

The variations of τ are much larger than the variations of the other values. However, most of the large values have errors that are as large or larger than the value itself, indicated by '$\sim$' in the table. Visually the $R(t)$ curves do not look fundamentally different from the others, thus any obvious problems with the measurements can be excluded. The largest value for τ without such a big uncertainty is 220 min for 31%. On the other hand it is important to consider the length of the measurement. The time scale for the laser irradiation was usually a few hours, so if the τ values are indeed so large, then the error on this parameter becomes of course large. To obtain more reliable values for τ the time scale for the measurement should be on the order of or larger than τ.

The parameter β does not follow a clear dependence on the power either. One problem here is that β and τ have similar effects in elongating the temporal behaviour of the resistance, so there is a certain correlation between those numbers. On the other hand, the values for β do not show any obvious irregularities even for those measurements in which τ becomes extraordinarily large. Furthermore the values for β agree with measurements from other groups [30] and plotting β and τ together does not reveal any clear correlation between the two.

Finally, ΔR is the combination of R_j and R_0 ($\Delta R = R_0 - R_\mathrm{j}$, which is equivalent to $\Delta R = R_0 - R_\infty$). The higher the jump in resistance R_j, the smaller becomes ΔR. And equivalently the larger R_0, the larger ΔR. This can easily be understood from figure 3.4. The highest values are achieved for the 27% measurement. This originates from the large R_0, since R_j here is not special compared to the other measurements. The negative values in ΔR for larger powers are due to the jump being larger than the amplitude of the

stretched exponential function, so the resistance is higher after illumination than before.

The large variation of the parameters leads to the question of how reliable the fits are. A global fit would not help in this case, since a non-trivial dependence of the parameters on the intensity is expected, due to the competition of the photoconductivity and the regeneration.

The main goal of these experiments was to measure the shift in T_c by measuring $R(T)$ curves before and after (or during) illumination. With regard to the values of table 3.4, 27% was chosen as the power setpoint to get the largest ΔR. A direct comparison of $R(T)$-curves is not conclusive. One problem is that the temperature fluctuations and drifts in the cryostat are on the order of the expected shift, and furthermore heating and cooling the film can always cause a small change in resistance, but perhaps too much for our small effect.

Nonetheless, a number can be calculated that one can interpret as a shift in T_c. From the $R(T)$ curve one can get a value for $\frac{\mathrm{d}R}{\mathrm{d}T}$. Then the change in temperature can be calculated by

$$\Delta T_\mathrm{c} = \left(\left.\frac{\mathrm{d}R}{\mathrm{d}T}\right|_{T_\mathrm{c}} \right)^{-1} \cdot \Delta R \tag{3.2}$$

which, with $\left.\frac{\mathrm{d}R}{\mathrm{d}T}\right|_{T_\mathrm{c}} = 0.333\,\Omega\,\mathrm{K}^{-1}$ (as one can see in figure 3.2) and $\Delta R = 2.1\,\mathrm{m}\Omega$, results in $\Delta T_c = 6.3\,\mathrm{mK}$ as the largest observed value.

It is not clear from this number whether the curve is shifted to the right or downwards. But since the $R(T)$-curve is approximately linear around T_c, the two interpretations are equivalent and it is thus justified to interpret this as a shift in T_c.

One fact that needs to be mentioned here is that in most publications the intensity is assumed to be irrelevant and that only the photon dose counts. For our measurements this is clearly not the case. One obvious problem is the increase of the jump height with increasing intensity. Another problem is the non-persistence of the photoconductivity here. So the decrease is in constant competition with the relaxation.

Setpoint [%]	Power [μW]	R_j [mΩ]	R_0 [mΩ]	τ [min]	β	ΔR [mΩ]
25	17.64	0.153(7)	0.307(6)	26.5(7)	0.57(1)	0.154(4)
27	43.73	0.329(7)	0.364(6)	12.0(2)	0.56(1)	0.035(3)

Table 3.3: The values for measurements with different powers at $T = 105\,\mathrm{K}$ and $\lambda = 850\,\mathrm{nm}$.

As a comparison to table 3.2, table 3.3 shows the values of two measurements with a wavelength of 850 nm. It is important to compare the powers to the ones in table 3.2 and not the setpoints. The measurements with setpoints 26% and 29% from table 3.2 are the closest in power to the two measurements in table 3.3. The main difference is that R_0 is smaller for 850 nm. This is consistent with the findings that the effect vanishes between 900 nm and 1000 nm. With the measurements performed it looks like the effect is larger for shorter wavelengths without having a clear cut and just getting weaker with increasing wavelength and finally disappearing for wavelengths longer than 1000 nm. Since the power is the same, the reason must be the difference in energy carried by photons of different wavelengths, or, from the viewpoint of the electromagnetic wave, the differences in the electric field. The wavelength range where the effect ceases to exist is comparable to other materials [18, 31]. It is also noteworthy that the jump height R_j is in agreement between the two wavelengths and it thus appears to only depend on the power incident on the sample, which gives further evidence that the jump R_j is only thermally induced.

T [K]	R_i [Ω]	R_j [mΩ]	R_0 [mΩ]	τ [min]	β	ΔR [mΩ]	ΔT [mK]
95	0.00770	-0.02(1)	0.089(7)	38(5)	0.40(4)	0.094(4)	10
100	0.152	0	0.57(1)	32(1)	0.217(5)	0.320(5)	5.6
105	0.995	0.25(3)	1.729(5)	24.7(2)	0.393(1)	1.226(1)	3.6
110	1.76	0	0.98(1)	5.47(8)	0.41(6)	0.833(4)	12
115	2.00	0	0.956(9)	4.6(1)	0.33(3)	0.751(1)	20
120	2.16	0	0.430(5)	2.67(7)	0.503(7)	0.369(1)	12
150	2.99	0	0.282(3)	25.7(5)	0.523(7)	0.279(1)	10

Table 3.4: The values for measurements with different temperatures at $\lambda =$ 650 nm. The shift ΔT was calculated using equation 3.2.

Measurements at different temperatures were performed for $\lambda = 650$ nm. Their values are shown in table 3.4. These measurements were done with the NKT laser that we bought, which is a slightly different model than the one used before, for example it has a higher maximum power. Furthermore to lower the expenses, no AOTF was bought and a grating monochromator was used that was already present.

As expected, the initial resistance R_i goes up with increasing temperature. The values for R_j are especially notable this time. For 95 K a small downwards jump was found that has not been seen in any other of our measurements. Other than that, only for 105 K a jump can be seen, all other R(T) curves are continuous, both for switching the laser on and off. β be-

haves again unpredictably, but τ gets smaller with increasing temperature except for the measurement at 150 K. There is also a relatively big jump between 105 K and 110 K, which is at T_c. This is shown in figure 3.8.

The values for R_0 and ΔR are also remarkable. For increasing temperature, they grow monotonically until they have their maximum at 105 K after which they decrease monotonically. It thus appears that T_c is indeed the best temperature to investigate photoconductivity in this material. It needs to be mentioned that if $R_j = 0$, then according to figure 3.4 one would expect $R_0 = \Delta R$, which is only approximately true in table 3.4. The reason for this is that R_0 and ΔR were calculated with different methods (R_0 is a fit parameter, ΔR is the difference of R_i and R_∞) and the fit tends to slightly overestimate R_0.

Temperature [K]	R_j/R_i [10^{-3}]	R_0/R_i [10^{-3}]	τ [min]	β	$\Delta R/R_i$ [10^{-3}]
95	-3(1)	11.6(9)	38(5)	0.40(4)	12.2(5)
100	0	3.75(7)	32(1)	0.217(5)	2.10(3)
105	0.26(3)	1.810(5)	24.7(2)	0.393(1)	1.284(1)
110	0	0.557(6)	5.47(8)	0.41(6)	0.474(2)
115	0	0.479(4)	4.6(1)	0.33(3)	0.3762(5)
120	0	0.199(2)	2.67(7)	0.503(7)	0.1706(5)
150	0	0.094(1)	25.7(5)	0.523(7)	0.0934(3)

Table 3.5: The same values as table 3.4, this time adjusted for the different initial resistances.

The higher values of R_i at higher temperatures could cause values of R_j, R_0, and ΔR to appear larger just because they behave relative to R_i. To exclude any such effects all resistances were normalized to R_i. This is shown in table 3.5. Now all resistances just decrease with increasing temperature, so probably one still gets more information from the non-normalized values.

According to Kudinov et al. [4] the time constant τ should depend on the temperature as

$$\tau(T) = \tau_0 \exp\left(\frac{\Delta}{k_B T}\right). \tag{3.3}$$

If one plots τ versus the inverse temperature in a plot with a logarithmic y-axis, the result should be a linear function. This is done in figure 3.8. One can clearly see that the points are not on a line. However, if one disregards the leftmost point, which corresponds to 150 K, then the points below T_c and those above T_c do follow a linear behaviour. The results from the fits to equation 3.3 are shown in table 3.6.

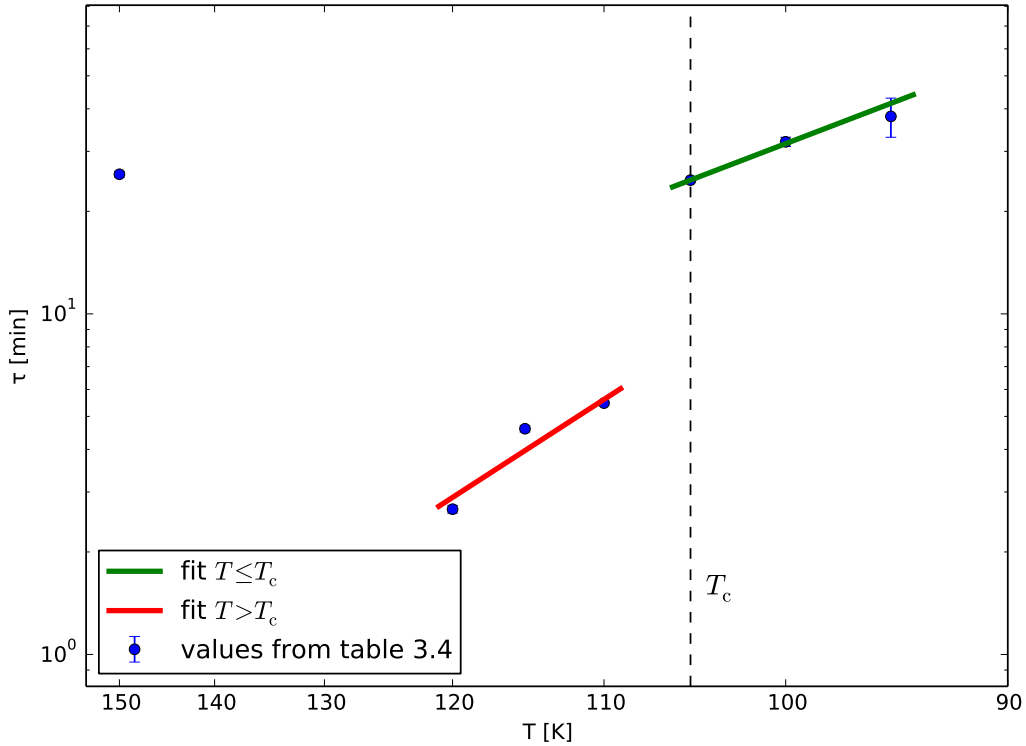

Figure 3.8: The time constant τ versus the inverse temperature. The green lines are fits according to equation 3.3. The vertical dashed line indicates T_c.

	τ_0 [min]	Δ [eV]
$T < T_c$	0.18(8)	0.045(4)
$T > T_c$	0.002(5)	0.08(2)

Table 3.6: The fit parameters for figure 3.8.

The values obtained do not agree well with the results by Kudinov, but the data points here are a bit sparse to really make a well-founded statement.

3.5 X-rays

A last test was conducted with an X-ray source. The maximal acceleration voltage of the source is 50 kV and the maximal current is 2 mA. The material of the target is tungsten. The attenuation length of $Bi_2Sr_2Ca_2Cu_3O_{10}$ as a function of energy is shown in figure 3.9. The spectrum of the X-ray source is displayed in figure 3.10. From this two graphs one can see that the majority of absorbed photons comes from the range between 7 keV and 12 keV, due to the high photon rate and the short attenuation length in this region.

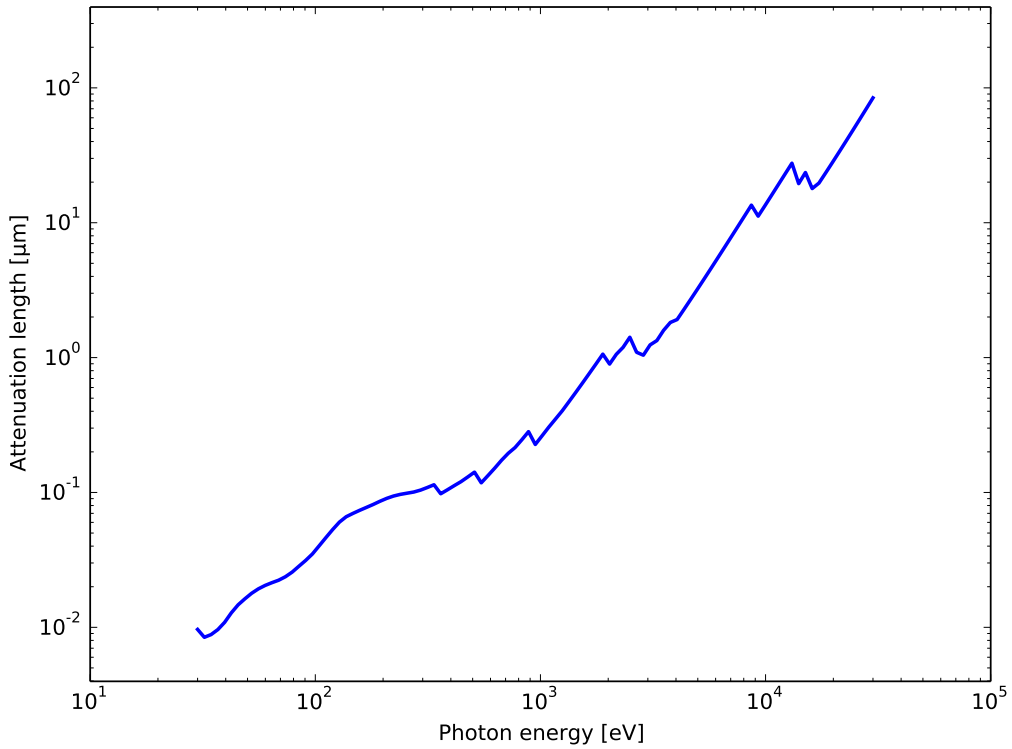

Figure 3.9: The attenuation length of X-ray photons as a function of energy. The data is taken from the CXRO [32].

A measurement with the X-ray source is shown in figure 3.11. It shows the resistance of the sample irradiated for almost an entire day. The maximal energy of the X-rays was 50 keV, the current was 2 mA and the temperature was 105 K.

The green curve is a fit of the stretched exponential function (Eq. 3.1). The agreement to the measured data is astounding, especially if the long measurement time is taken into account. The parameter values of the fitted

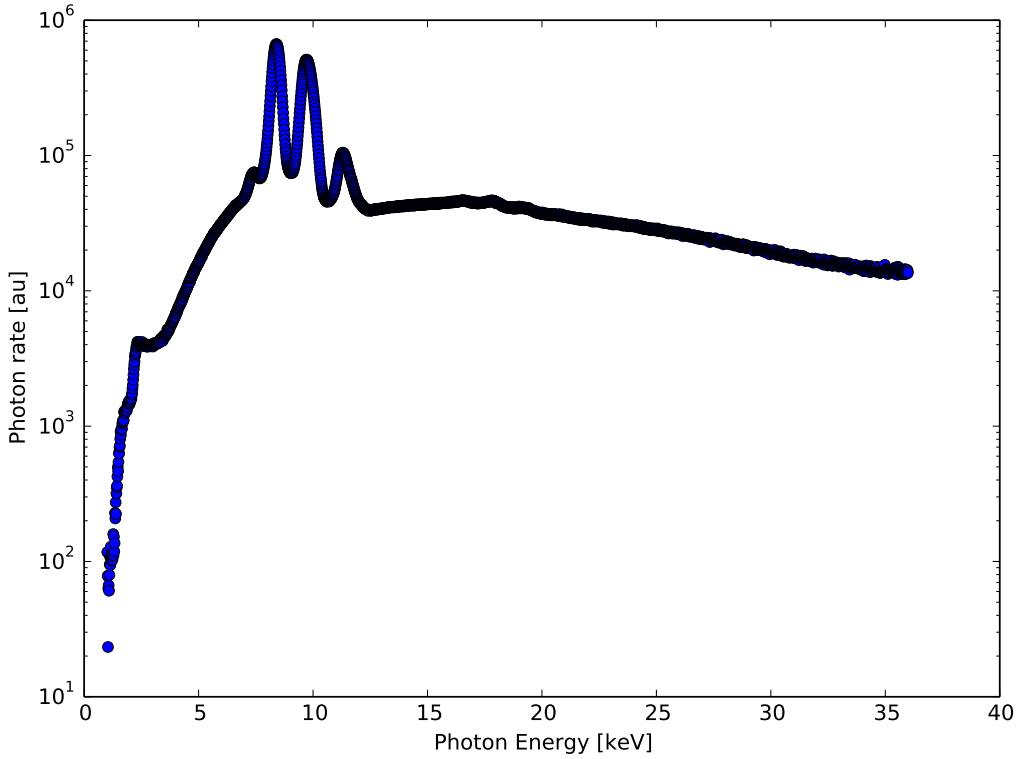

Figure 3.10: The spectrum of the X-ray source. The high energy part up to 50 keV *could not be detected by the sensor.*

function are $R_0 = 2.6795(7)\,\mathrm{m\Omega}$, $\tau = 5.999(2)\,\mathrm{h}$, and $\beta = 0.9828(4)$. The jump height when turning the X-rays on is $\approx 0.83\,\mathrm{m\Omega}$ and the jump when turning it off is $\approx 0.55\,\mathrm{m\Omega}$. It is noteworthy that β is very close to 1, which would then correspond to a normal exponential function. The shift in the critical temperature can be calculated again using equation 3.2, with the result of ΔT_c =6.4 mK.

The most remarkable difference to the earlier measurements is the appearance of strong persistent photoconductivity. After an irradiation for one day, waiting for multiple days did not increase the resistance to a value close to the initial level. A measurement showing the regeneration of the resistivity is shown in figure 3.12. It is the regeneration after an irradiation equivalent to the one shown in figure 3.11. Over a course of a day, only a small increase of $0.4\,\mathrm{m\Omega}$ can be seen. The next irradiation can then at most reduce the resistance for the same $0.4\,\mathrm{m\Omega}$. During the last few hours the resistance does not increase any further. This might be caused by temperature fluctuations.

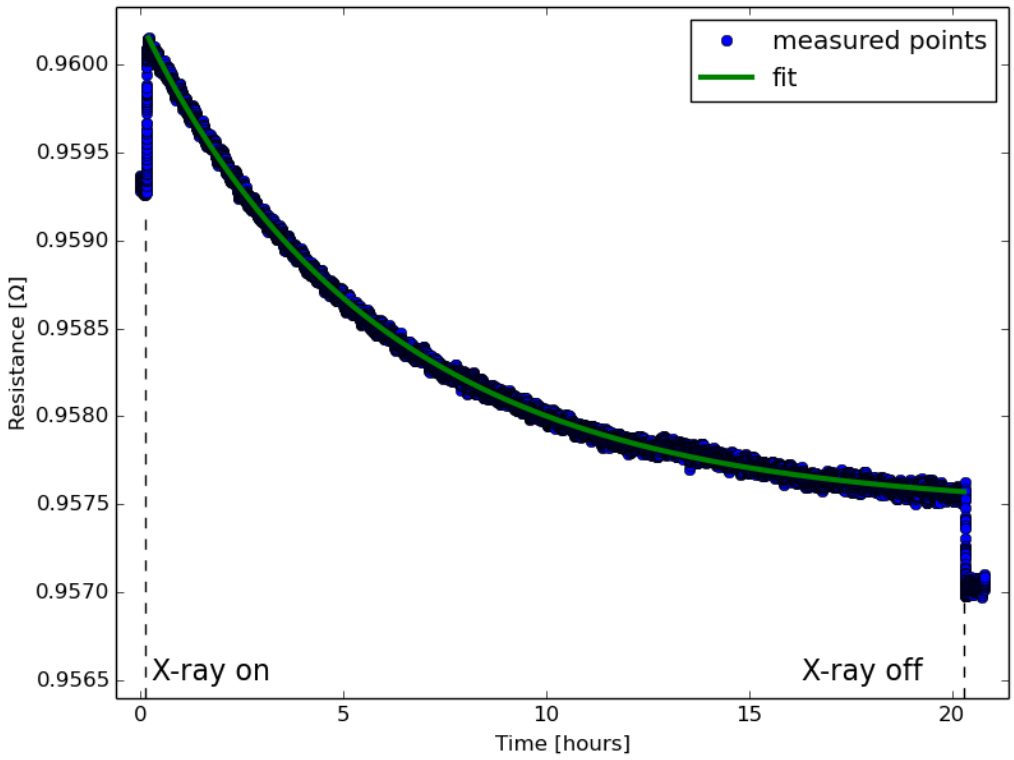

Figure 3.11: This figure shows the resistance measurement during irradiation with X-rays of energies up to 50 keV*. The measurement lasted for almost an entire day. The fit of the stretched exponential function is in perfect agreement with the data. The temperature was* 105 K*.*

The regeneration of 0.4 mΩ corresponds to approximately 16% of the total resistance increase needed for a full regeneration.

In order to accelerate the regeneration process, the film was heated to higher temperatures. Tests were made for 110 K, 115 K, 120 K. We found that 2 h at 120 K is already enough to regenerate the film noticeably, the lower temperatures are not yet enough. Waiting at 120 K for half a day fully regenerates the film and the subsequent measurement shows again a behaviour similar to before the irradiation.

The different behaviour in the time-scale, the function behaving almost exponential, and the more persistent photoconductivity can all be explained by assuming that a different mechanism is involved in the photocoductivity when using x-rays instead of light of longer wavelengths.

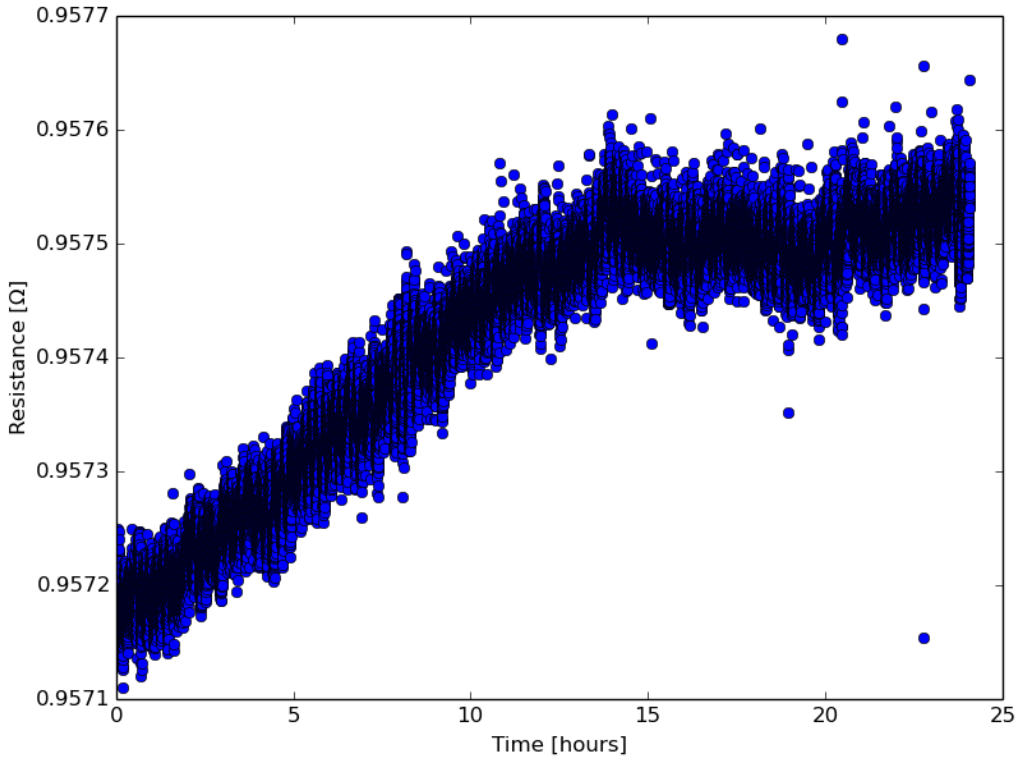

Figure 3.12: The regeneration of the resistance over one day. The temperature was constant at 105 K.

Part II

Effects of Electron and Neutron Irradiation on the BEC in Magnetic Dimer Systems

Chapter 4

Scientific Background

4.1 Introduction

Systems of particles can exist in a number of different states, some of them with peculiar properties. One of these states is the Bose-Einstein condensate (BEC), which is a state of matter that can occur for bosonic particles. In this state, a significant fraction of the bosonic particles can condense into the ground state. This fraction is much larger than what is expected from thermal considerations. For fermionic particles, by contrast, due to the Pauli exclusion principle, a certain state can only ever be occupied by at most one particle (two particles if one neglects the spin).

So far Bose-Einstein condensation has been observed in a multitude of systems, the most famous being ^{4}He [33, 34] and cold atomic gases [35, 36]. The systems studied in this thesis are magnetic insulators, where bosonic quasiparticles called triplons undergo Bose-Einstein condensation. The Bose-Einstein condensation of triplons was discovered in $TlCuCl_3$ in 1999 [37] and interpreted as such a short time later [38]. It should be mentioned here that, although this phenomenon is called Bose-Einstein condensation, some important properties of certain BECs, such as superfluidity, have not been found so far.

The decisive feature in these materials is a dimer of spin $\frac{1}{2}$ atoms. These two spins form a spin-singlet ($S = 0$) as their ground state due to an antiferromagnetic interaction, and can occupy the higher-lying triplet states ($S = 1$) in the presence of a magnetic field due to the Zeeman splitting of these states, or through thermal excitation. These bosonic spin-triplets are the triplons that can undergo Bose-Einstein condensation.

An atom within the dimer will interact with the other atom in the dimer (intradimer interaction), as well as with the other dimers (interdimer interac-

tion). The intradimer interaction is stronger than the interdimer interaction and it is negative, causing an antiferromagnetic alignment.

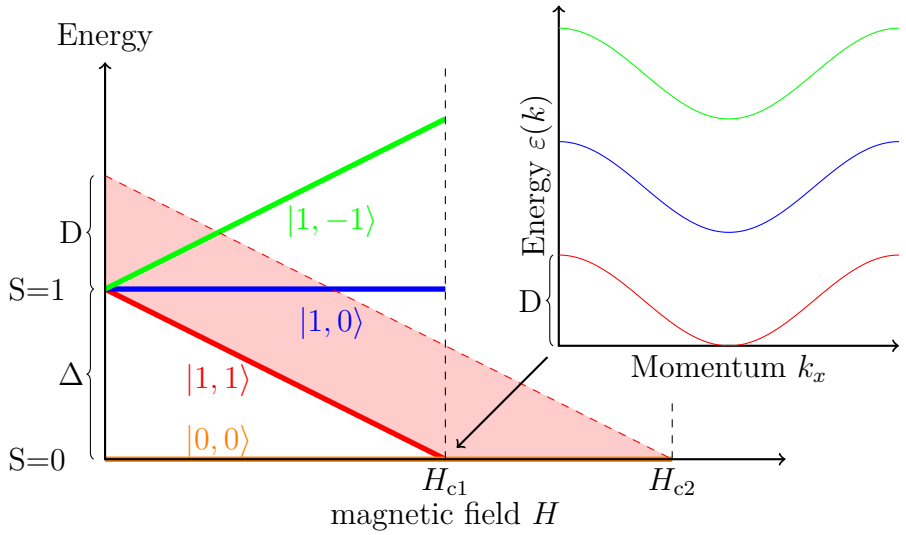

Figure 4.1: The Zeeman splitting of the $S = 1$ excited state. This state is separated from the $S = 0$ state by an energy gap Δ. An applied external magnetic field causes the threefold degenerate state to split (green, blue, red). Due to the dispersion relation of the triplets they are distributed over an energy band (shown in the inset). The red area shows the energy distribution of the band of bandwidth D. At the field H_{c1} the part of the band with lowest energy intersects the energy level of the $S = 0$ state (orange). The state of lowest energy is now a superposition of a $|1,1\rangle$ state and a $|0,0\rangle$ state.

The process of the "condensation" through the Zeeman effect is shown in figure 4.1. Initially, two energy levels exist, an $S = 0$ level with energy E_0 and a triply degenerate $S = 1$ level with energy $E_1 = E_0 + \Delta$. At this time the $S = 0$ level is the ground state and thermally excited dimers can enter the triplet state. The triplets are subject to a dispersion relation with a bandwidth of D. Applying an external magnetic field causes the $S = 1$ state to split into three states with different energies. The energy of the state with its spin magnetic moment aligned to the magnetic field decreases with an increasing field. At a field strength H_{c1} the lowest energy in the dispersion relation of this state is equal to E_0. At even higher field strengths it is then energetically favourable for the dimers to be in the $|1,1\rangle$ state. An increasing field will lower the energy for a larger fraction of the triplet band below the energy of the $S = 0$ state. This continues until at H_{c2} the highest energy in the triplet band falls below E_0. At this point all dimers occupy a $|1,1\rangle$ state.

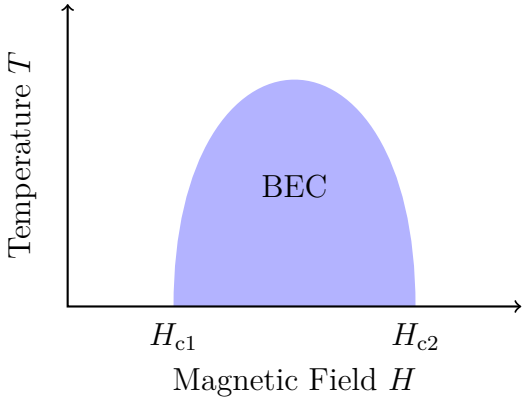

Figure 4.2: The phase diagram for a magnetic insulator. The Bose Einstein condensate is present between H_{c1} and H_{c2} at low temperatures.

In a magnetic phase diagram the BEC phase has a dome-like shape between H_{c1} and H_{c2}. This is shown in figure 4.2. Close to the quantum critical points, i.e. $T = 0$, the phase boundary can be described by a power law. Near H_{c1} it is given by

$$T_c \propto \Big(H - H_{c1}\,(T = 0)\Big)^{\phi}. \tag{4.1}$$

An equivalent expression is valid near H_{c2}. The value for the exponent is $\phi = \frac{2}{3}$ for a three dimensional system. The critical temperature for these systems (on the order of Kelvin) is much larger than for atomic gases (on the order of nanokelvin) due to the small effective mass of the triplons and their large density.

The magnetic moment of the system for $T = 0$ is 0 for $H < H_{c1}$, increases linearly for $H_{c1} < H < H_{c2}$ and is one μ_B per dimerized atom for $H > H_{c1}$. This is shown in figure 4.3. From this picture it can also clearly be seen, that the triplon density is linear in the field for $H_{c1} < H < H_{c2}$ and one can interpret the field as the chemical potential.

Since every dimer site occupies either a singlet state or a triplet state, a good description of the system is obtained by approximating the wavefunction as $|\psi\rangle_i = \alpha_i(H)\,|0,0\rangle_i + \beta_i(H)\,|1,1\rangle_i$ [39].

The BEC quantum phase transition has already been observed in many different materials. For the present work $TlCuCl_3$, $Sr_3Cr_2O_8$, and $Ba_3Cr_2O_8$ have been used, but there exist more complicated materials, too, such as $(C_4H_{12}N_2)Cu_2Cl_6$ [40].

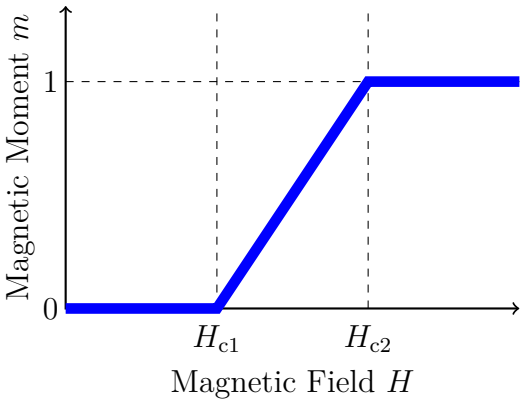

Figure 4.3: The magnetic moment as a function of the magnetic field at a temperature of 0 K*. The magnetic moment is per dimerized atom and per* μ_B*.*

4.2 The Role of Disorder

The main goal of the second part of this thesis is to investigate the influence of disorder on the Bose-Einstein condensation in spin dimer magnets.

Previous experiments were aimed at chemically substituting some atoms in different materials, such as $TlCuCl_3$ and $Ba_{3-x}Sr_xCr_2O_8$.

In the case of $TlCuCl_3$, potassium is added during the growth of the crystals resulting in $Tl_{1-x}K_xCuCl_3$. Both parent compounds $TlCuCl_3$ and $KCuCl_3$ are coupled dimer systems, with a difference in the strength of the interactions. In $TlCuCl_3$ the coupling is strong, while in $KCuCl_3$ the coupling is weaker [41].

In $Tl_{1-x}K_xCuCl_3$, variations are found in the magnetic behaviour that go beyond a simple averaging of the parent compounds [42]. The susceptibility as a function of temperature does not decrease towards zero temperature and its maximum is broadened.

These behaviours indicate that the ground state is not a spin singlet, but rather a magnetic state with continuous excitations. The absence of a Brillouin term for low temperatures and the almost linear dependence of the magnetic moment on the field indicates that the spins are strongly coupled.

The transition temperature decreases with increasing K content and falls below 1.8 K even for 7 T somewhere between $x = 0.16$ and $x = 0.36$. The critical exponent is independent of x, and the critical field decreases for increasing x up to $x = 0.08$ and is constant afterwards. The phase boundary, however, shifts strongly with increasing x by decreasing the rise in T for increasing magnetic fields. This is shown in figure 4.4.

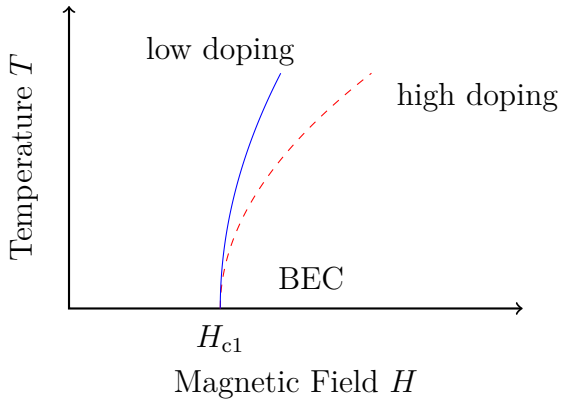

Figure 4.4: The dependence of the phase boundary of the BEC on K doping in $Tl_{1-x}K_xCuCl_3$.

From $m(H)$ data one can deduce that the average interdimer interaction does not change with x and that the decrease of T_c is due to the randomness in exchange interaction induced by the partial substitution of Tl by K. In the picture of the Bose-Einstein condensation, the difference in intradimer interaction caused by Tl and K leads to a random on-site potential that causes the triplons to localize in a process described by Anderson localization. The localization suppresses the formation of a Bose-Einstein condensate by preventing the bosons from forming a coherent state.

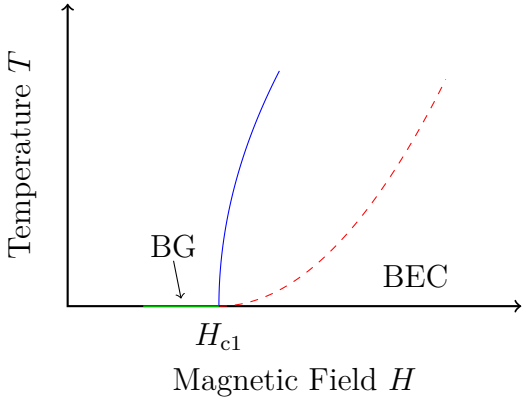

Figure 4.5: The shape of the phase boundary of the BEC without disorder (blue) and with disorder (red, dashed), leading to the Bose glass phase (BG, green).

Another study even claims the discovery of a so-called Bose glass phase below H_c in $Tl_{1-x}K_xCuCl_3$ [43], partly in disagreement with earlier results [42].

This phase is indicated by a different exponent in equation 4.1. The tangent of the phase boundary then becomes parallel to the magnetic field axis instead of perpendicular to it as expected for $\phi = \frac{2}{3}$. This is shown in figure 4.5. Another study investigated the chemical substitution of the magnetic Cu ions by non-magnetic Mg ions [44]. Here the doping leads to an impurity-induced magnetic ordering.

The effects of disorder have been studied theoretically, for example by Rakhimov et. al. [45]. Their investigations show that the random potential leads to a uniform renormalization of the system parameters. The magnetization data of $Tl_{1-x}K_xCuCl_3$ can be explained qualitatively by this theory. The δ-correlated disorder is found to decrease the critical temperature, while interparticle interactions do not influence the critical temperature in the approaches considered due to boson-boson repulsion. A further cause for the decrease in the critical temperature can be the increase of the effective mass of the triplons.

An experimental problem arises from the structural changes accompanying a chemical substitution. One would like to investigate the influence of a pure disorder potential, but in real experiments chemical disorder always changes the lattice parameters and as such the properties of the system as a whole. The entangling of the disorder potential with other effects thus hinders the experimental studies. Introducing point defects by means of irradiation could be a way to eliminate the influence of changing bond lengths and interactions upon chemical substitution.

4.3 Detection

Various ways exist to probe the Bose-Einstein condensation in these materials. One example is neutron scattering, which can be used to measure, among other things, the Zeeman splitting and the dispersion relation [46].

Another method to detect the Bose-Einstein condensation is to measure the magnetic moment as a function of the temperature and the magnetic field. This is the main method used in this work. In practice the magnetic moment is measured either as a function of temperature or magnetic field. Distinct features in these curves allow one to pinpoint the phase transition. Another method is the measurement of the heat capacity [49]. The disadvantage here is that the feature in the measurement curves are less pronounced for smaller fields and can only be clearly seen for very high fields $H \gtrsim 7\,\mathrm{T}$.

By using electron spin resonance (ESR), the antiferromagnetic alignment can be observed as well as the spin gap below H_c [47]. Nuclear magnetic resonance (NMR) is another technique used to investigate spin dimer sys-

tems [48]. Even sound attenuation can be used to probe these materials [50]. In the condensed state the thermal conductivity should be enhanced drastically, which makes its measurements a further possible method [51].

4.4 Mathematical Description of the magnetic moment

The temperature dependence of a paramagnetic sample with non-interacting localized spins is well known to follow the shape of the Brillouin function

$$B_J(x) = \frac{2J+1}{2J}\coth\left(\frac{2J+1}{2J}x\right) - \frac{1}{2J}\coth\left(\frac{1}{2J}x\right), \tag{4.2}$$

where J is the total angular momentum and

$$x = \frac{g\mu_\mathrm{B}JB}{k_\mathrm{B}T} \tag{4.3}$$

is the ratio of the magnetic energy and the thermal energy. The total magnetic moment is then given by

$$m_\mathrm{p} = N_\mathrm{p} g\mu_\mathrm{B} J B_J(x), \tag{4.4}$$

where N_p is the number of paramagnetic atoms in the sample.

In the case of coupled spin dimer systems, the magnetization for $x \ll 1$ follows the so called Bleaney-Bowers formula given by

$$m_\mathrm{d} = N_\mathrm{d} \cdot \frac{g^2\mu_\mathrm{B}^2 B}{J' + k_\mathrm{B}T\left(3 + \exp\frac{J_0}{k_\mathrm{B}T}\right)}. \tag{4.5}$$

Here N_d is the number of dimerized atoms in the sample, J' and J_0 are interaction constants. J' is the effective interdimer interaction containing all the interactions to other dimers. J_0 is the intradimer interaction.

It needs to be mentioned that the original Bleaney-Bowers formula usually does not contain the term J'. This is true in the case of noninteracting dimers. In the case of interacting dimers, however, this term needs to be taken into account.

In a perfect sample of dimers one would only observe the Bleaney-Bowers function, but of course in a real material one will always have defects and impurities, and thus the total observed magnetization is given by the sum of the paramagnetic and the dimer term:

$$m_\mathrm{tot}(T, B, N_\mathrm{p}, N_\mathrm{d}, J_0, J') = m_\mathrm{p}(T, B, N_\mathrm{p}) + m_\mathrm{d}(T, B, N_\mathrm{d}, J_0, J'). \tag{4.6}$$

The total number of magnetic atoms in such a sample is $N_{\mathrm{tot}} = N_{\mathrm{p}} + N_{\mathrm{d}}$. Further contributions may also be present, such as diamagnetism or ferromagnetism. These contributions should, however, not contribute beyond a simple constant shift, at least for low temperatures.

Chapter 5

Experimental Setup

5.1 Samples

Three already thoroughly examined materials exhibiting the Bose-Einstein condensation of triplons are $TlCuCl_3$, and the two isostructural materials $Sr_3Cr_2O_8$, and $Ba_3Cr_2O_8$. These are the ones investigated in this work, with the main focus on $TlCuCl_3$. $Sr_3Cr_2O_8$ and $Ba_3Cr_2O_8$ were fabricated at the University of Zurich, the samples of $TlCuCl_3$ were prepared by K. Krämer from the University of Bern.

$TlCuCl_3$ has four formula units per unit cell. The crystal has a monoclinic $P2_1/c$ space group with lattice parameters a = 3.982 Å, b = 14.144 Å, c = 8.890 Å and $\beta = 96.32°$ [41]. The Cu_2Cl_6 structures in the bc-plane are surrounded by 6 Tl atoms. The Cu_2Cl_6 chains then extend in the direction of the a-axis.

The spin gap in $TlCuCl_3$ is $\Delta = 0.650\,\mathrm{meV} \mathrel{\widehat{=}} 7.54\,\mathrm{K}$ and $B_c = 5.5\,\mathrm{T}$ [37]. It is thus one of the few materials in which the BEC can be observed with comparably cheap and standard laboratory equipment. Other materials usually require very high magnetic fields that are only achievable in high field laboratories.

The materials $Sr_3Cr_2O_8$ and $Ba_3Cr_2O_8$ have a hexagonal lattice and the structure can be described using the space group $R\bar{3}m$. The lattice constants for $Ba_3Cr_2O_8$ are a = 5.757 Å and c = 21.388 Å [54]. For $Sr_3Cr_2O_8$ these values are a = 5.562 Å and c = 20.221 Å [55], so that $Sr_3Cr_2O_8$ has a smaller unit cell than $Ba_3Cr_2O_8$. Each Cr ion is surrounded by an oxygen tetrahedron, and couple to another Cr atom to form dimers in the direction of the c axis.

5.2 SQUID

The device used to measure the magnetic moment was a MPMS XL by Quantum Design. Its most important part is a SQUID, which stands for superconducting quantum interference device. SQUIDs are the most sensitive detectors for magnetic fields available [56].

The SQUID consists of a superconducting ring with two Josephson junctions incorporated. One important quantum mechanical phenomenon that a SQUID makes use of is the flux quantisation through a superconducting ring. A change in the magnetic field through the ring will cause a current to flow to adjust the flux to an integer multiple of the flux quantum. Sudden changes in this current due to changes of the quantized magnetic flux are accompanied by a voltage that can be measured by the electronics attached to the SQUID. A SQUID thus works as a flux-to-voltage transducer.

The sample is moved up and down through four pickup coils arranged in a second order gradiometer configuration [57]. The current induced in these coils by the magnetic flux flows through a wire to a smaller input coil that then creates a magnetic field next to the actual SQUID. A change in magnetic flux through the SQUID will then induce the voltage variations. Measuring the SQUID voltage as a function of position in the pickup coils then allows for the calculation of the magnetic moment.

5.3 Neutron Irradiation Facility

The neutron irradiation was performed at the Paul Scherrer Institute (PSI) in the NAA[1] at the spallation neutron source SINQ. The samples are placed in polyethylene containers and transported through a tube system to a position close to the target. A second facility, the PNA[1], reaches a higher neutron flux, however, the handling is more complicated.

Figure 5.1 shows the neutron flux as a function of energy at the two facilities PNA and NAA. The majority of neutrons are thermal neutrons with energies of 10 to 100 meV. For our experiment we used the NAA. The total flux there is $10^{13}\,\mathrm{cm}^{-2}\,\mathrm{s}^{-1}$. The neutrons are produced by directing 590 MeV protons on a target made of lead rods enclosed in a zirconium alloy. It is positioned inside a heavy water moderator tank to decrease the neutron energy [59].

[1] Historically NAA and PNA used to be abbreviations for 'Neutron Activation Analysis' and 'Präparative Neutronen Aktivierung'. However, these days the abbreviations just stand for themselves as they have lost their meaning.

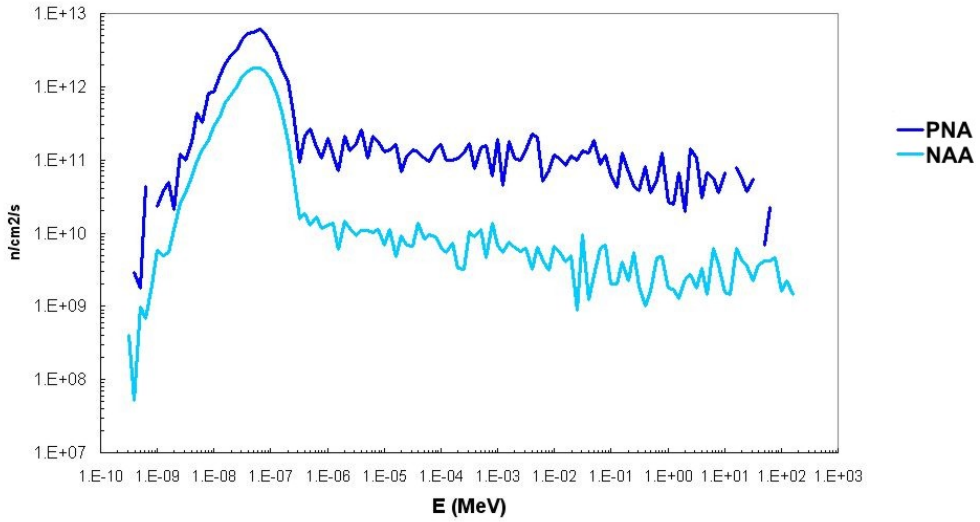

Figure 5.1: The neutron flux for the NAA and the PNA as a function of the neutron energy. Our irradiation was done in the NAA. Image from PSI [58].

After the chosen time of irradiation has been reached, the capsule is transported back to the lab. At this point our samples were always too radioactive to be taken back directly to the university to continue with the measurements. After a waiting time of several weeks the level of radioactivity was low enough for the samples to be sent back to the University of Zurich. During the waiting time the samples were stored in a dry environment (except for the first test when we did not yet know that the deactivation would take so long).

Chapter 6

Measurements

6.1 Electron Irradiation of $TlCuCl_3$

The electron irradiation was performed by BGS Beta-Gamma-Service GmbH & Co. KG in Germany. The Electron Energy was 10 MeV and the absorbed dose was 1000 kGy. To prevent a strong heating of the sample the irradiation was performed in multiple steps.

The unit gray (Gy) is defined as absorbed radiation energy per mass, i.e. $1\,\mathrm{Gy} = 1\,\mathrm{J\,kg^{-1}}$. The mass of the sample used here was 0.0453 g, leading to a total absorbed energy of $\approx 45\,\mathrm{J}$.

The stopping power for any material can be obtained from a NIST database [52]. The curve of the stopping power for $TlCuCl_3$ is shown in figure 6.1. For 10 MeV electrons the stopping power is $2.219\,\mathrm{MeV\,cm^2/g}$. With a density $\rho = 4.995\,\mathrm{g/cm^3}$ this yields an energy loss of the electrons of $11.08\,\mathrm{MeV\,cm^{-1}}$. The sampe thickness was on the order of 1 mm, so the energy loss per electron should amount to the order of 1 MeV. The samples were not of a uniform shape and the electron energy decreases inside the sample, but due to the relatively low energy loss inside the sample, they can be regarded as uniformly irradiated.

The dose was chosen to be as high as possible while still being feasible and affordable, and is comparable to those found in publications about inducing defects in semiconductors [53].

The magnetic moment as a function of temperature of the sample before and after irradiation with electrons is shown in figure 6.2. The magnetic moment is in units of μ_B and per copper atom. It was measured for 11 different external magnetic fields from 6 T to 7 T in steps of 0.1 T. The temperature was scanned from 1.8 K to 4 K in steps of 0.04 K.

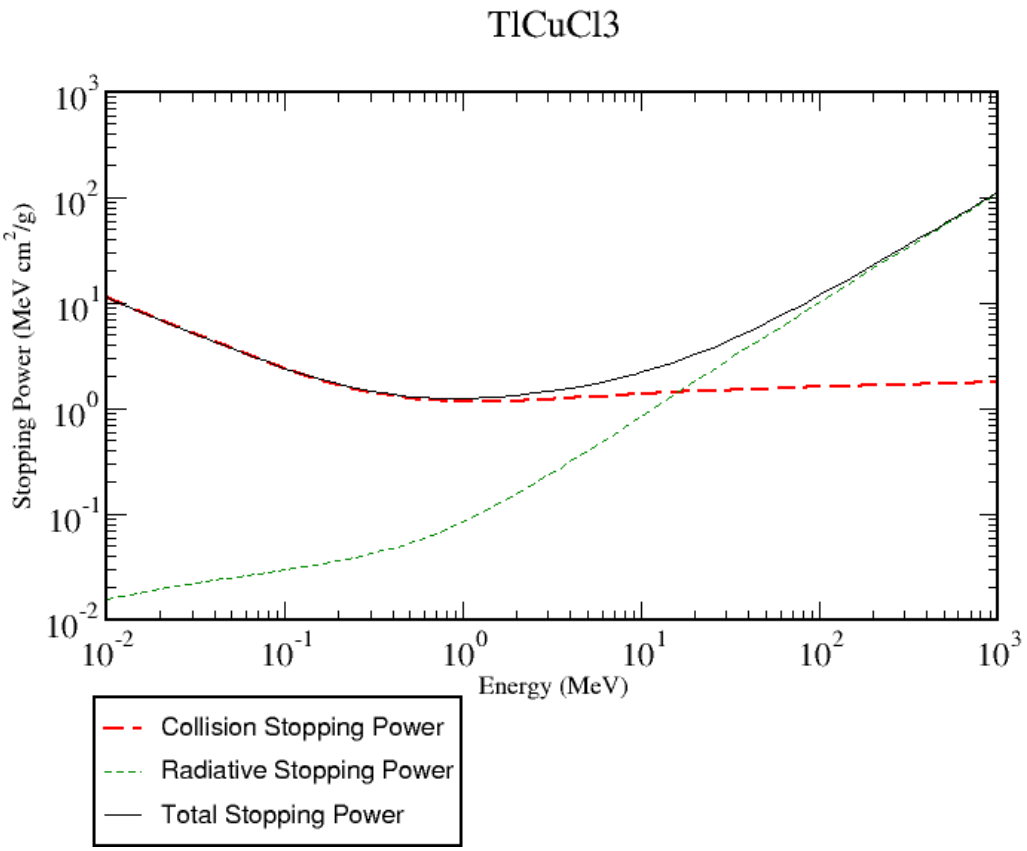

Figure 6.1: This figure shows the curve for the stopping power for $TlCuCl_3$ from the NIST database [52]. The 10 MeV *electrons used are close to the minimum. The stopping powers due to collision and radiative loss are shown seperately. Together they form the total stopping power.*

The plot shows the data as recorded by the SQUID. The moments of the irradiated sample are shifted towards lower or even negative moments. This is interpreted as being due to different backgrounds, mainly a strong diamagnetic background in the measurement after the irradiation. These different backgrounds are most likely caused by the capsules and the cotton used to hold the sample in place and are therefore not significant.

Furthermore a small shift of the local minimum of T_c can be seen. The shift of T_c is approximately 0.1 K towards lower temperatures after the irradiation. This shift is, however, too small to be unambiguously attributed to the irradiation because of the dependence of T_c to the direction of the crystal. The crystal was positioned in the same position before and after irradiation as well as possible. We assume the deviation to be no more than 20°.

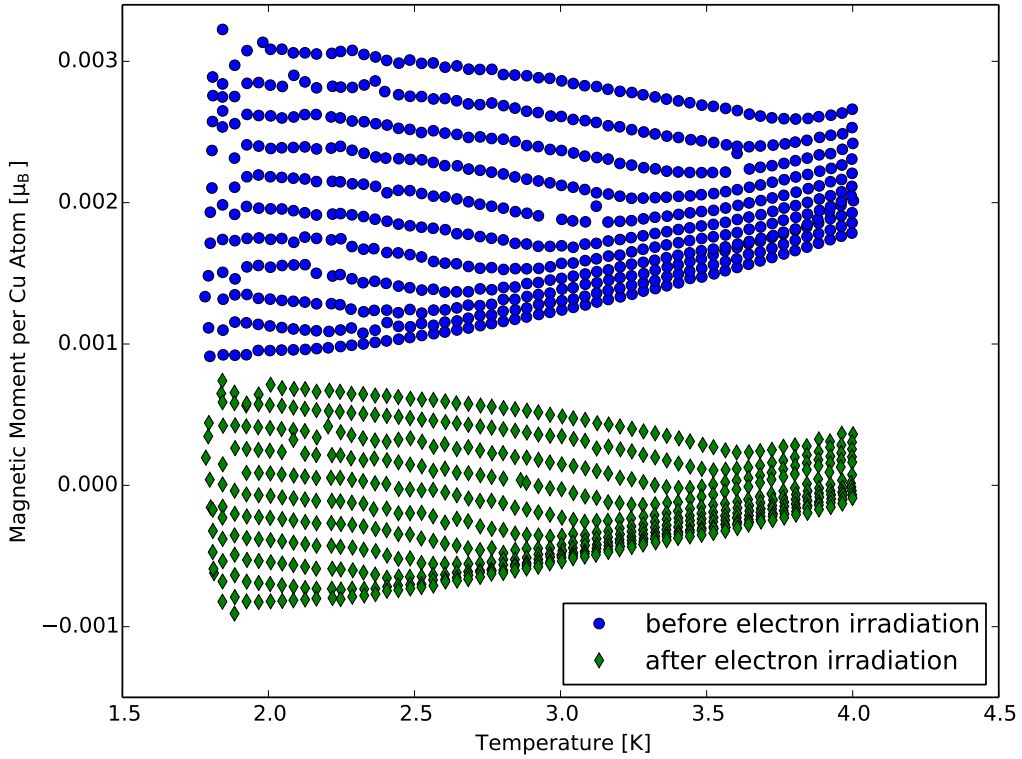

Figure 6.2: The magnetic moment of $TlCuCl_3$ as a function of temperature for different fields before and after the electron irradiation. It shows the original, unaltered data. The shift is most likely due to different backgrounds.

No further electron irradiations were performed after this first test. The main reason is the dose, which was already extremely high for the company involved, and the cost for a longer irradiation would increase linearly. This is mainly due to the heat generation in the sample, which would make multiple shorter irradiation sessions necessary.

6.2 Neutron Irradiation of $TlCuCl_3$

In total, we had the samples three times irradiated for three different amounts of time and thus three different fluences. The first run lasted 10 min, the second 4 min, and the third 30 min. The doses reached this way are comparable to what was used in other studies [60]. Reports where higher doses were used can also be found in the literature, and it was first our intention to achieve these higher doses. However, we observed already signs of decomposition at the lower doses mentioned above, and we continued to use those.

Natural copper consists mainly of 69% ^{63}Cu and 31% ^{65}Cu [61]. The neutron capture cross section is approximately 5 b and 1 b, respectively [62]. Thallium consists of 30% ^{203}Tl and 70% ^{205}Tl with cross sections of 9 b and 0.1 b. Chlorine comprises 76% ^{35}Cl and 24% ^{37}Cl with cross sections of 20 b and 0.3 b. Since $TlCuCl_3$ consists of three times more Cl than Tl and Cu and chlorine having the largest cross section, most neutrons should be captured by chlorine.

By capturing a neutron, the nucleus becomes unstable and decays radioactively. In case of α and β decay, a new type of atom will be created at the site of the old one, hopefully causing the desired random potential without changing the lattice parameters too much.

By multiplying the flux with the cross section and the irradiation time one can calculate the fraction of converted atoms. For a cross section of one barn and 30 min of radiation the result is 2×10^{-8}.

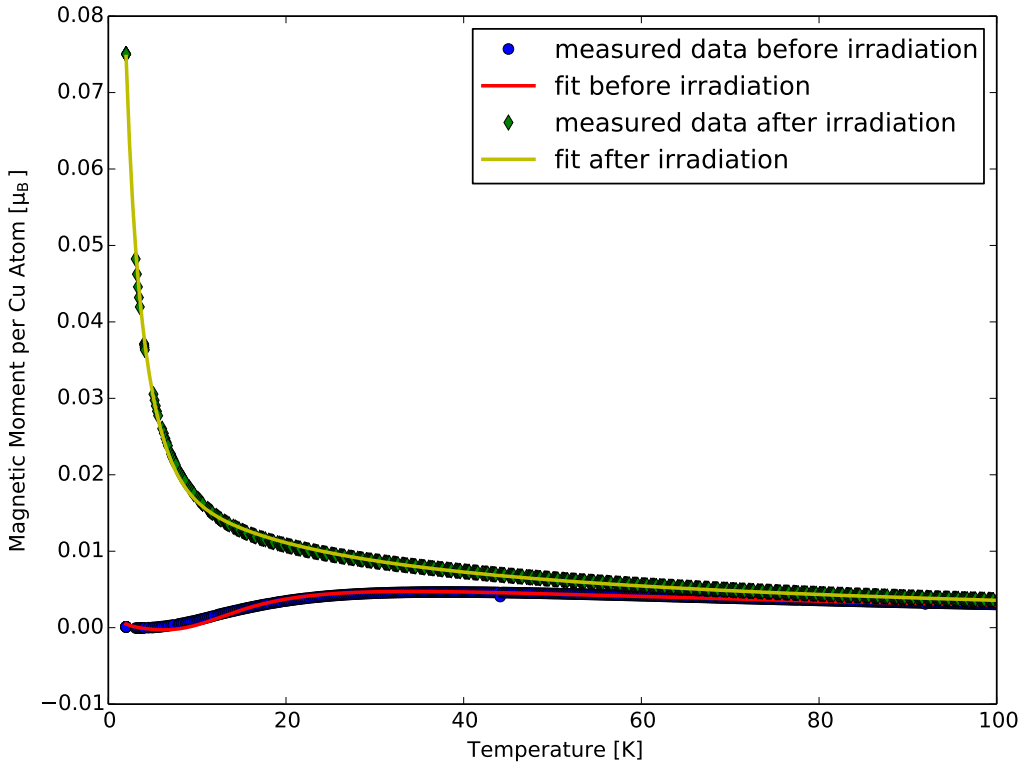

Figure 6.3: The $m(T)$ measurement of the $TlCuCl_3$crystal for a field of 1 T *before and after neutron irradiation for* 10 min *from* 2 K *to* 100 K.

The first run, which lasted 10 min, was originally intended to test the radioactivity in the samples as preparation for an irradiation that was planned

quantity	before	after
N_p	$2.04(8) \times 10^{17}$	$1.246(1) \times 10^{19}$
N_d	$4.52(8) \times 10^{19}$	$3.8(1) \times 10^{19}$
J_0/k_B	55.3(1) K	45.9(2) K
J'/k_B	149(6) K	210(10) K

Table 6.1: Results from fitting the magnetization $m(T)$ of $TlCuCl_3$ using equation 4.6, before and after neutron irradiation for 10 min.

to last for an entire day. We found that the sample had become almost completely paramagnetic, which is shown in figure 6.3, the corresponding parameters according to equation 4.6 are shown in table 6.1. At first we assumed that we overestimated the needed dose for the irradiation and performed another test lasting only 4 min. The sample for the second run was pressed from a powder, i.e. it was not monocristalline. We also included a sample of $Sr_3Cr_2O_8$ and $Ba_3Cr_2O_8$ (see next section).

quantity	before	after
N_p	$2.23(2) \times 10^{18}$	$2.24(2) \times 10^{18}$
N_d	$7.2(1) \times 10^{19}$	$6.5(1) \times 10^{19}$
J_0/k_B	54.1(2) K	54.0(2) K
J'/k_B	103(7) K	96(7) K

Table 6.2: The values of the fitted functions for $TlCuCl_3$ before and after neutron irradiation for 4 min.

The magnetization curve for the powder for 1 T is shown in figure 6.4, and the corresponding parameters of the fits to equation 4.6 are given in table 6.2. The g-factor used here was 2.23 [37], different values did not improve the fit. This value is only valid for $\mathbf{H} \perp (1, 0, \bar{2})$, for $\mathbf{H} \parallel b$, $g \approx 2.06$ [37].

The fit does not agree well with the data. Since these measurements were performed on a powder sample and all measurements with crystals show better agreement, it can be assumed that a powder is not described well enough by equation 4.6. In this figure it is clearly visible that the irradiation did not destroy a large fraction of the dimers. The difference in irradiation time could not cause this difference in destruction of dimers. It was thus concluded that the first crystal was destroyed by the air moisture. Indeed, during all runs, except the first one, the sample was in a bag with silica beads to absorb any humidity.

The 1 T measurements from 2 K to 300 K before and after irradiation for 30 min are shown in figure 6.5. The corresponding fit parameters are shown in

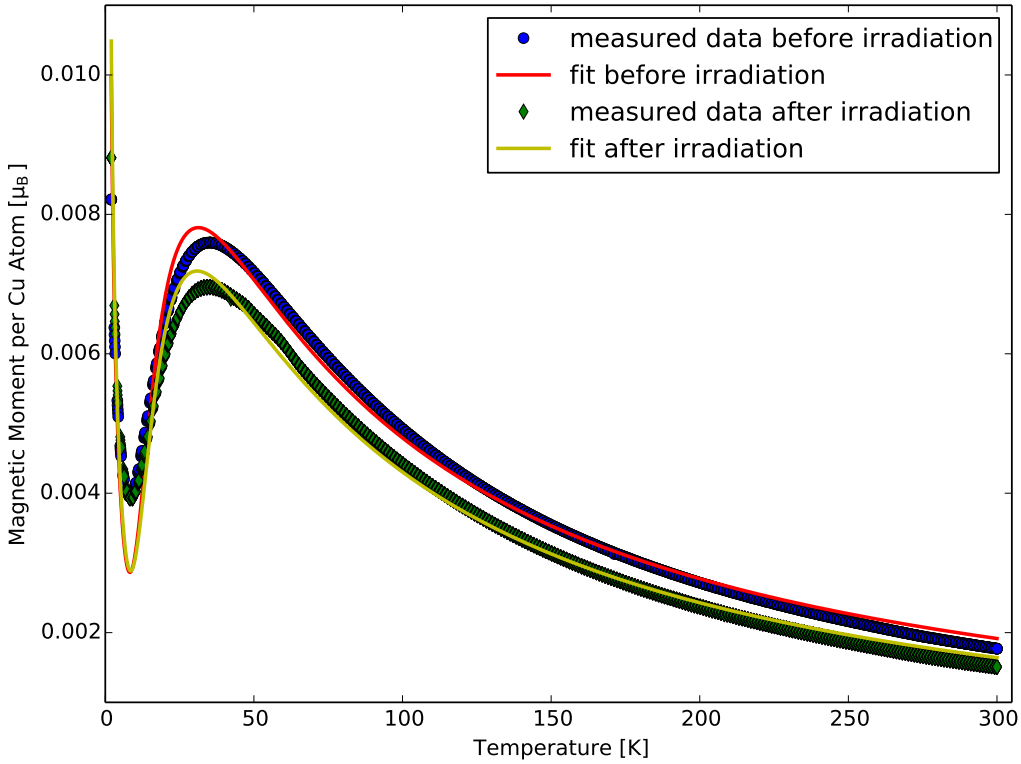

Figure 6.4: The $m\,(T)$ measurement of a $TlCuCl_3$ powder sample for a field of $1\,\mathrm{T}$ *before and after neutron irradiation for* $4\,\mathrm{min}$ *from* $2\,\mathrm{K}$ *to* $300\,\mathrm{K}$.

quantity	before	after
N_p	$3.61(9) \times 10^{17}$	$1.02(1) \times 10^{18}$
N_d	$6.73(7) \times 10^{19}$	$7.34(7) \times 10^{19}$
J_0/k_B	$55.34(8)\,\mathrm{K}$	$55.25(8)\,\mathrm{K}$
J'/k_B	$118(3)\,\mathrm{K}$	$123(3)\,\mathrm{K}$

Table 6.3: The values of the fitted functions for $TlCuCl_3$ before and after neutron irradiation for $30\,\mathrm{min}$.

Table 6.3. The fits agree better with the measured data this time. However, both the number of dimerized atoms and the number of paramagnetic atoms increase which makes a direct comparison of destroyed dimers and created paramagnets difficult. On the other hand, the number of paramagnetic atoms triples while the number of dimerized atoms increases by only 10%. This indicates the induction of paramagnets through the irradiation.

The m(T) measurements of $TlCuCl_3$ in magnetic fields larger than H_c before and after the 30 min neutron irradiation are shown in figure 6.6. Here,

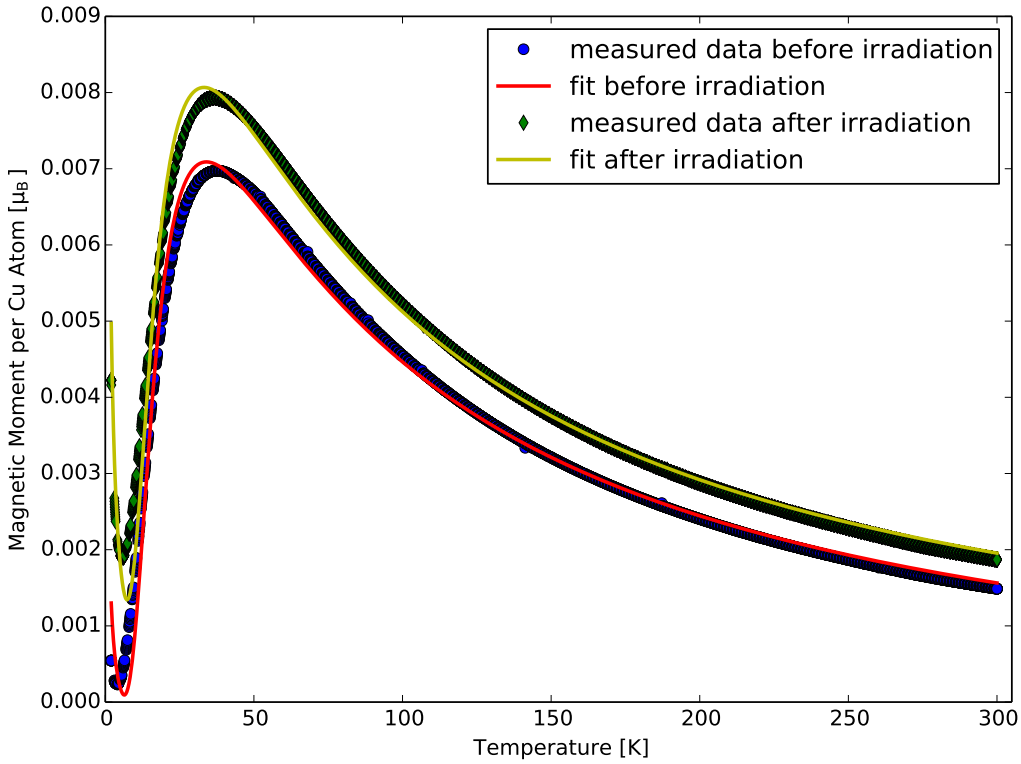

Figure 6.5: The $m\,(T)$ measurement of $TlCuCl_3$ for a field of 1 T *before and after neutron irradiation for* 30 min *from* 2 K *to* 300 K.

the magnetic field is large enough to induce the Bose-Einstein phase transition. The relative vertical position of the three data sets is arbitrarily chosen for clarity. The data before the irradiation had to be measured partly with a piece of iron put next to the sample to increase the values for the magnetic moment upwards, since the software controlling the measurement did not find the correct values for magnetic moments close to 0.

From these data a larger shift in the critical temperature upon irradiation can be seen. For example, for 7 T the shift is approximately 0.7 K towards higher temperatures. This is quite remarkable. To exclude a change in orientation to account for this change, the sample was rotated twice, but the change in T_c due to different orientation was found to be on the order of 0.2 K.

Another method to find the phase boundary is to measure $m(H)$ at fixed T (in the plots, $B = \mu_0 H$ is given). This was unfortunately not done before the irradiation. Nevertheless, the measurement was performed with the irradiated sample.

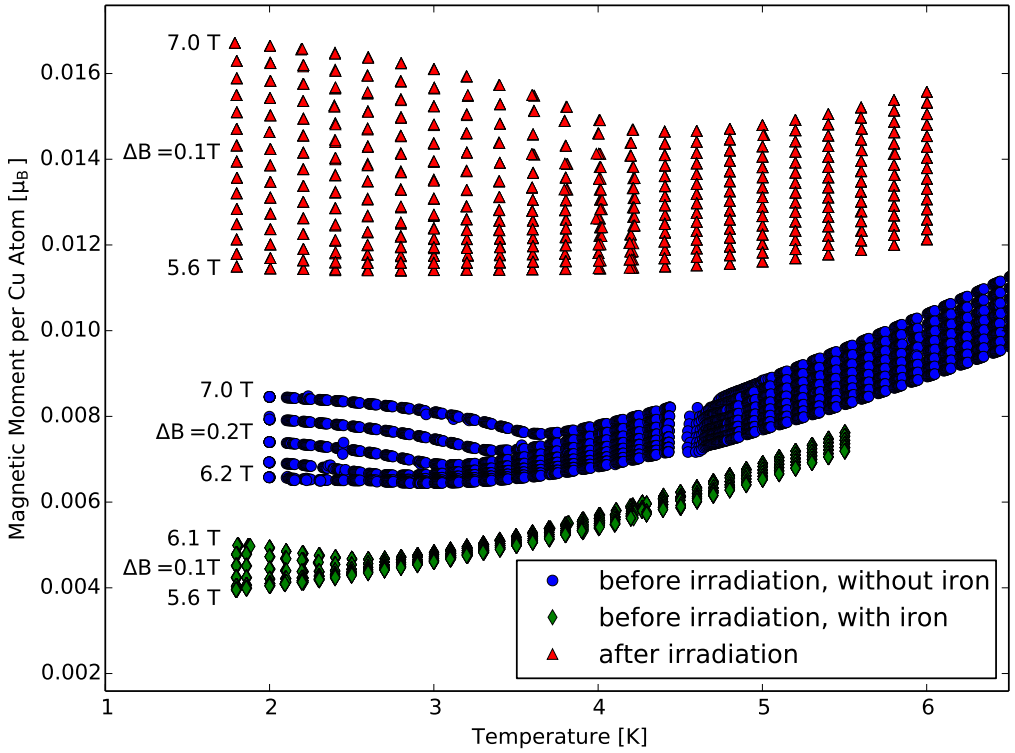

Figure 6.6: The magnetic moment as a function of temperature for $TlCuCl_3$ before and after neutron irradiation for 30 min. *As the three data sets have three largely different offsets to 0, they were shifted vertically for clarity.*

These $m(H)$ measurements for $T = 1.8\,\mathrm{K}$ are shown in figure 6.7. The external magnetic field was swept from 0 T to 7 T in steps of 0.01 T. For each field the magnetic moment was measured six times. The white points represent these unaltered points as measured by the SQUID. For fields close to the kink at H_c a lot of points lie far away from the mean value of the six points for every field. In order to obtain less scattered data, the mean and standard deviation of the six points for every field were calculated and then all points deviating more than 1.5σ were neglected. With the remaining points, a new mean was calculated. The result are the blue points in the plot. Simply calculating the running average of the white points was not sufficient to obtain such a smooth curve.

The critical field is located at the kink, i.e. at approximately 5.6 T. The reasons why the magnetic moment is not 0 below H_c are the facts that $T > 0$ and the presence of a paramagnetic background. Above H_c the magnetic moment follows closely a linear function, as expected.

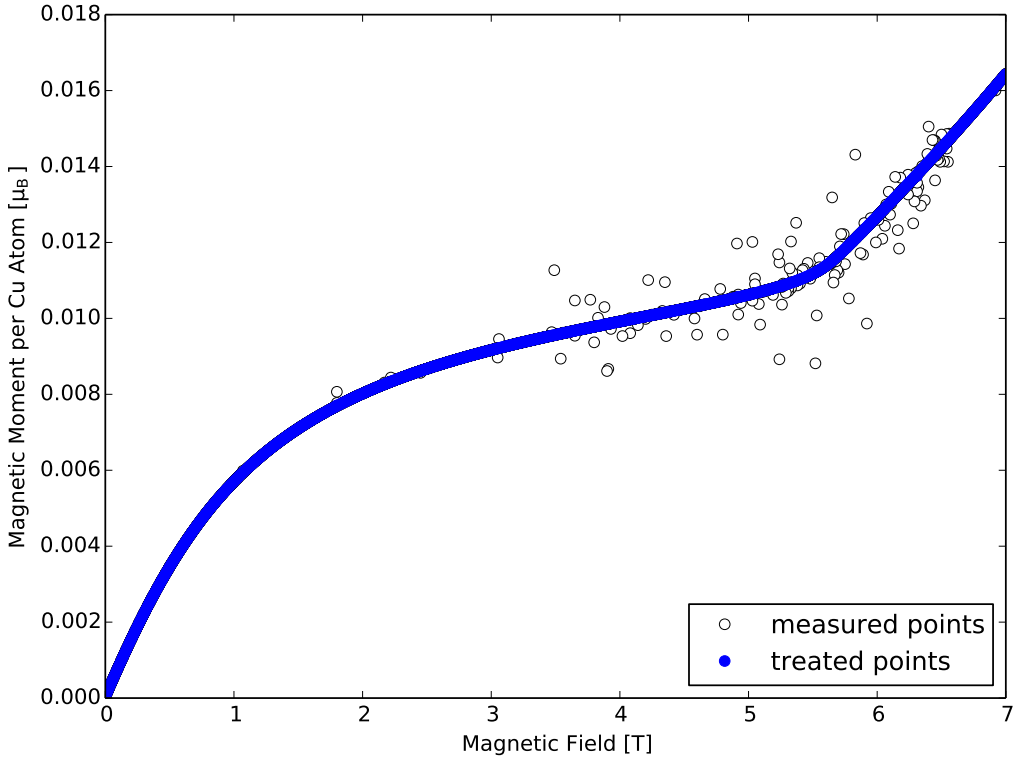

Figure 6.7: The $m(H)$ measurement at a temperature of 1.8 K *is shown here. The field is given in tesla as $\mu_0 H$. The white points are the measured points, the blue points are edited to remove all points far from the 'real' line. Most of the white points can not be seen as they lie directly beneath the blue points.*

Figure 6.8 shows the derivative of the magnetic moment $\mathrm{d}m/\mathrm{d}B$. The white points are the derivative as calculated from the blue points in figure 6.7. The yellow points are the same as the white ones, except all outliers neglected. The blue points finally are the yellow points smoothed over 11 points by a running average.

Finally, figure 6.9 shows the second derivative $\mathrm{d}^2m/\mathrm{d}B^2$. The white points are calculated from the blue line from figure 6.8. The blue points are again a smoothed version over 11 points of the white points. They serve as a guide to the eye and are not used any further. The peak between 5 T and 6 T around H_c can clearly be seen in the datapoints. In the following, the slowly varying background was assumed to follow a linear function in the region around the peak.

The peak itself shows similiarities to a Gaussian distribution

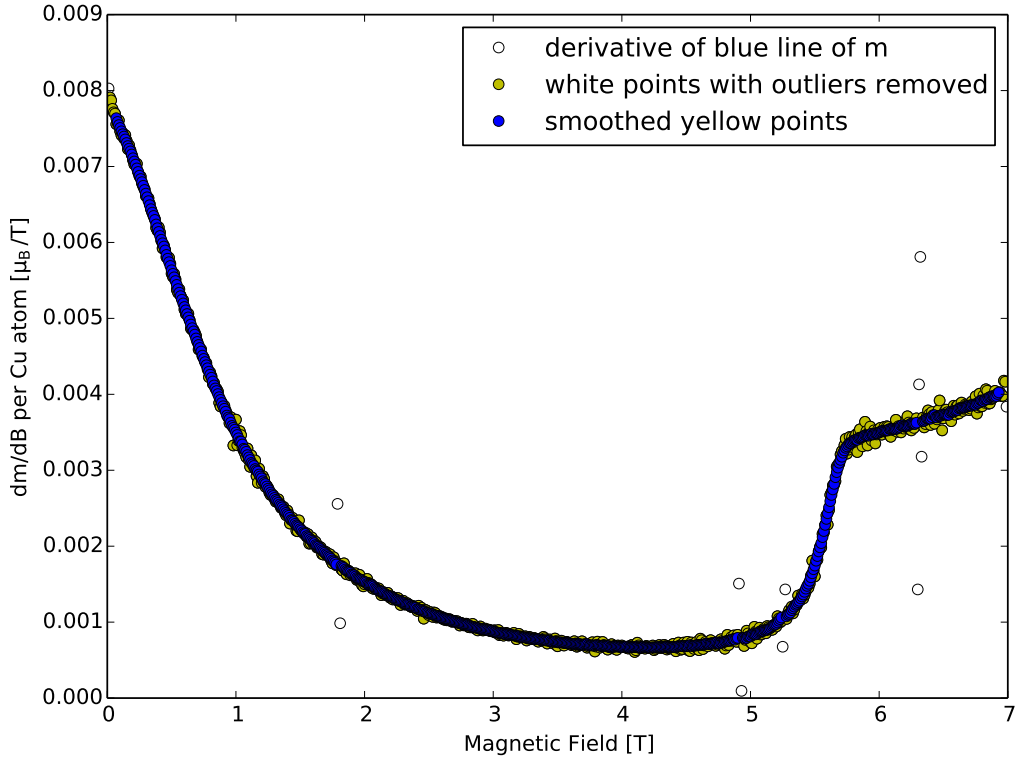

Figure 6.8: The derivative $\mathrm{d}m/\mathrm{d}B$ *of the magnetic moment from figure 6.7 with respect to the magnetic field.*

$$g(x) = \frac{1}{\sqrt{2\pi}\sigma} \exp\left(-\frac{x^2}{2\sigma^2}\right). \tag{6.1}$$

Upon close inspection one can see that the low field side (left) is expanded as compared to the high field side (right). First attempts using an asymmetric Gaussian function did not prove to agree well with the data. Further attempts with other functions were made and it turned out the data can be accurately described by a Gaussian distribution, convoluted with an exponential distribution

$$e(x) = \lambda \exp\left(-\lambda x\right) \cdot H(x), \tag{6.2}$$

where $H(x)$ denotes the Heaviside step function.

The convolution $f = g * e$ of the functions 6.1 and 6.2 can be written as:

$$f(x) = \frac{\lambda}{2} \cdot \exp\left(-x\lambda + \frac{(\sigma\lambda)^2}{2}\right) \cdot \operatorname{erfc}\left(\frac{-x + \sigma^2\lambda}{\sqrt{2}\sigma}\right), \tag{6.3}$$

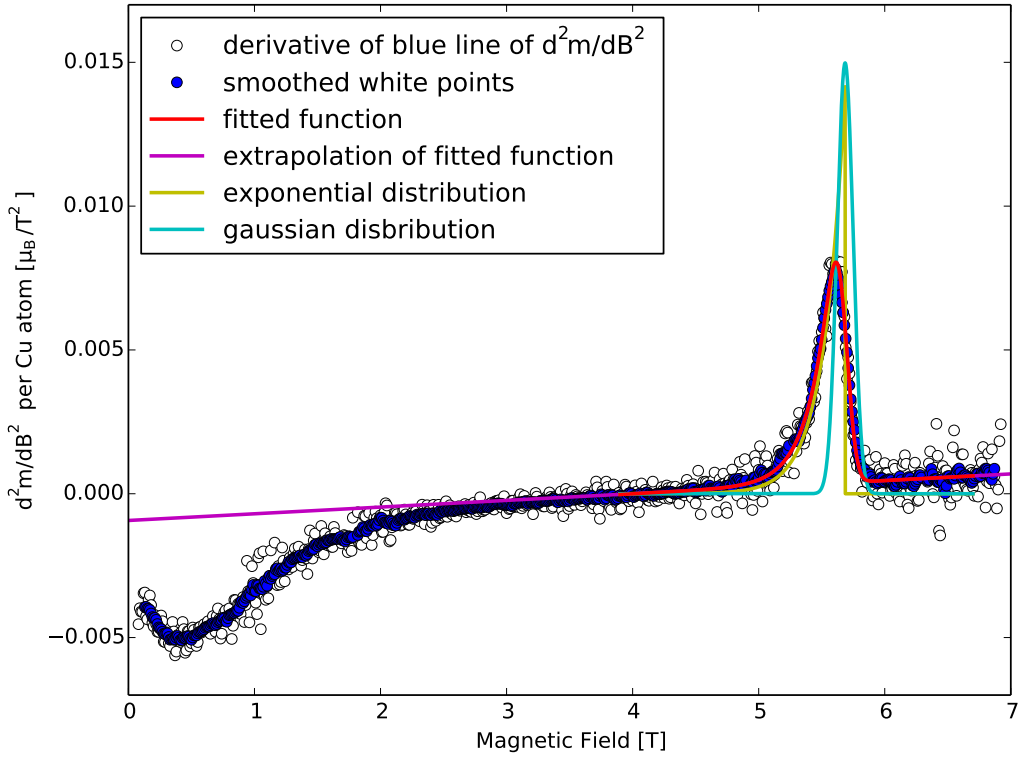

Figure 6.9: Second derivative of the magnetic moment $\mathrm{d}^2m/\mathrm{d}B^2$. *The red curve shows the fitted function according to equation 6.4. The magenta curve is the extension of the red curve beyond the fitted region. The exponential distribution is shown in yellow, the Gaussian distribution in cyan.*

where erfc() denotes the complementary error function.

This function $f(x)$ needs to be mirrored at the y-axis and shifted to B_e, the cutoff of the Heaviside function. Since the distribution 6.3 is normalized to an area of one, it needs to be multiplied by a scale factor s. Furthermore the linear background needs to be added. This then yields the function

$$\tilde{f}(B) = s \cdot \frac{\lambda}{2} \cdot \exp\left((B - B_e)\,\lambda + \frac{(\sigma\lambda)^2}{2}\right) \cdot \operatorname{erfc}\left(\frac{B - B_e + \sigma^2\lambda}{\sqrt{2}\sigma}\right) + aB + b. \tag{6.4}$$

The red line in figure 6.9 shows the fit of the data according to equation 6.4. It was fitted to the white data over the entire range where the red function is displayed. The magenta line is the continuation beyond the fitted region. It shows the deviation from the linear background valid for larger

fields. The yellow curve is the exponential distribution and the cyan curve the Gaussian distribution centered at the same field value.

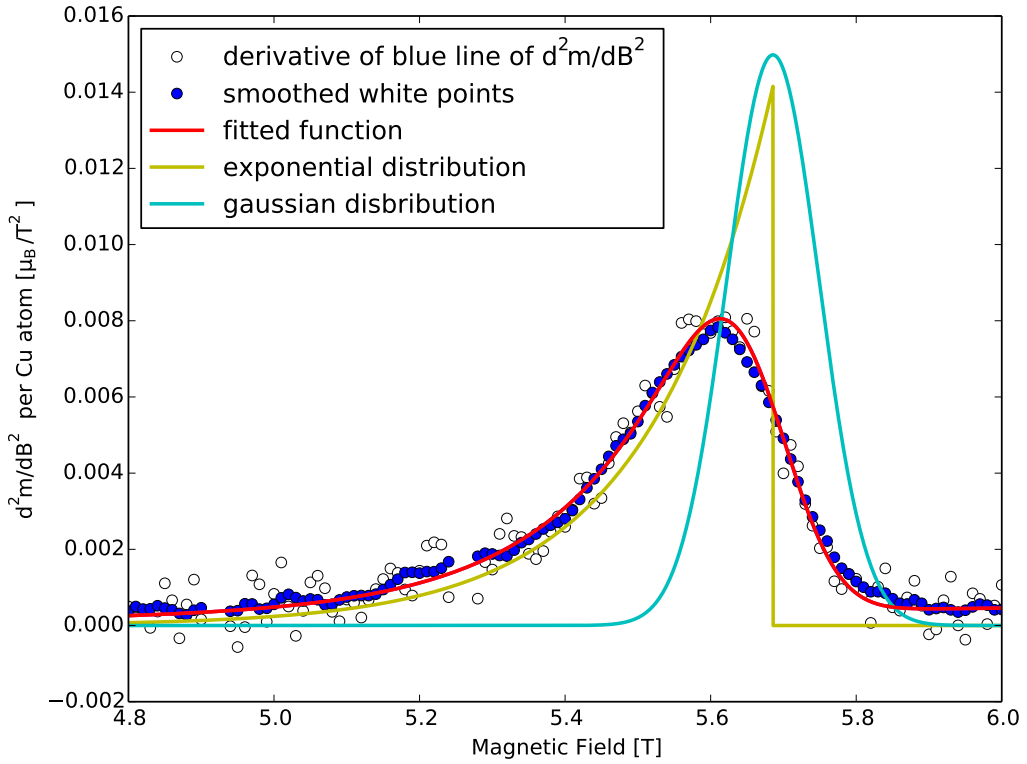

Figure 6.10: This image shows the same data as figure 6.9, zoomed in around the peak of the data.

In figure 6.10 we show the same data as in figure 6.9, zoomed in to the region around the peak. The agreement between the fitted function and the data is remarkably good. The interesting values from the fit are $\lambda = 5.8(3)\,\mathrm{T}^{-1}$, $\sigma = 62(4)\,\mathrm{mT}$, $B_e = 5.686(3)\,\mathrm{T}$. The maximum of the red curve is at 5.613 T.

The convolution of an exponential and a Gaussian distribution may be interpreted in two different ways. One way is to look at it as an exponential rise in the second derivative of the magnetic moment smeared out by fluctuations following a Gaussian distribution. This shifts the peak to lower values than what the end of the exponential given by the Heaviside step function would be. It is interesting to note that the integral of an exponential function is again an exponential function, so the curves of m and $\mathrm{d}m/\mathrm{d}B$ should then both be exponential up to B_e, too. Additionally the integration would yield a constant and a linear term for $\mathrm{d}m/\mathrm{d}B$ and m, respectively. In this interpre-

tation, the critical field would correspond to the cutoff-field ($B_c = B_e$). The second way to look at it is that the real feature is a Gaussian peak centred at B_e and that it is smeared out in an exponential way. Since this function is not based on a physical model but merely heuristically, it is unclear which one of the two interpretations is true.

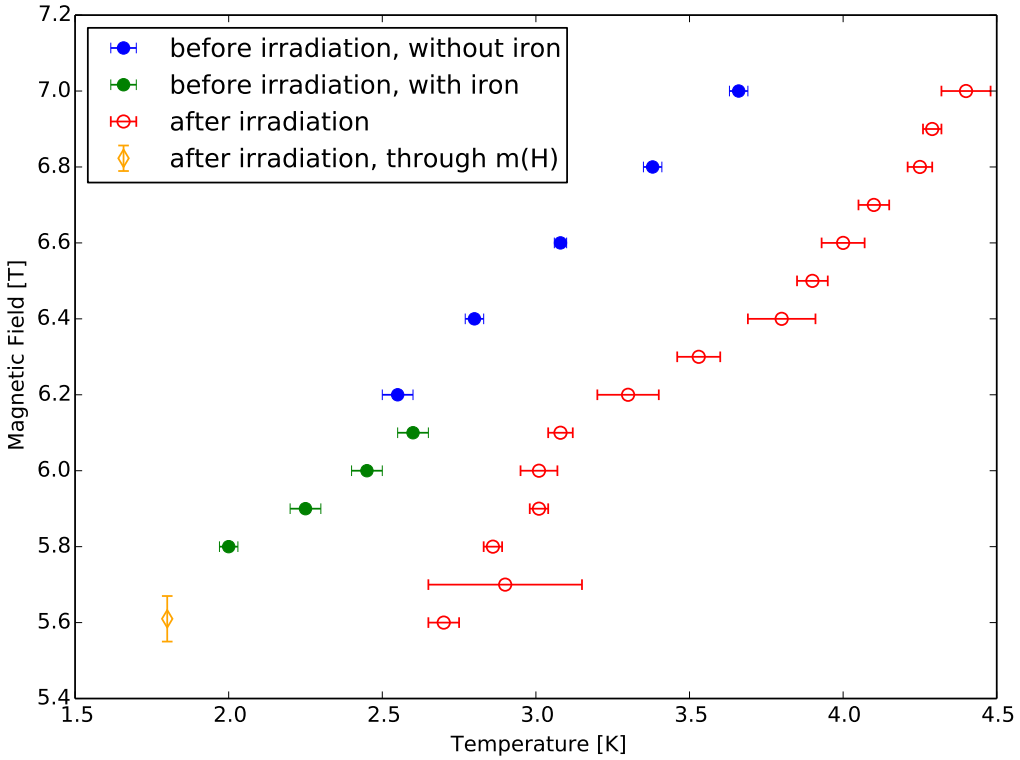

Figure 6.11: The phase diagram of our $TlCuCl_3$ sample before and after irradiation with neutrons for 30 min. *The circle-shaped points are taken from $m(T)$ measurements, the diamond-shaped point is from the $m(H)$ measurement. Filled symbols are before the irradiation, empty symbols are after the irradiation.*

From the $m(H)$ and the $m(T)$ measurements we can draw a phase diagram to compare the phase boundaries before and after the neutron irradiation. This phase diagram is shown in figure 6.11. The blue and green points represent the measurements before the irradiation, blue the ones without iron, green the ones with iron. Other than a small shift they agree very well to one another and to the expected behaviour as measured by various other groups. The red points are measured after the irradiation. The data points shown in figure 6.11 are the temperatures at which the curves in figure 6.6

are at their minimum for each corresponding field value. The most obvious change is the fairly large decrease of the critical field for any given temperature, or from an alternative viewpoint, the increase of the critical temperature for a given magnetic field. The shift in the field is approximately 0.4 T. The shift in temperature is approximately 0.9 K. Another important change in the shape of the phase boundary is the appearance of an apparent kink in the slope. At approximately 3.2 K the slope of the irradiated curve suddenly changes. A possible explanation would be the involvement of an additional phase in the irradiated sample. This means that around 3.2 K and 6.1 T three different phases would meet in a tricritical point. Originating from this point,an additional phase boundary should then lie somewhere left of the red points. This additional phase should, in principle, manifest itself in the $m(T)$ or $m(H)$ curves by an additional feature. If one inspects the curves in figures 6.6, 6.7, 6.8, and 6.9 in search for a sign of an additional phase transition, no indications for a further phase transition can be found, however.

From the $m(H)$ measurements performed after the irradiation one can obtain an additional point of the phase boundary, which is indicated by a yellow diamond in figure 6.11. It is the field value corresponding to the maximum of the fitted curve in figure 6.9. It agrees better with the data taken before the irradiation than with those taken after the irradiation. This raises the question whether the experimental data for the red points are interpreted correctly.

6.3 Neutron Irradiation of $Sr_3Cr_2O_8$ and $Ba_3Cr_2O_8$

The neutron irradiation was also performed on $Sr_3Cr_2O_8$ and $Ba_3Cr_2O_8$. The critical fields at which Bose-Einstein condensation occurs in these materials is higher than what our laboratory equipment can provide, so the only measurements made for these materials were the 1 T temperature scans to examine the dimerized and paramagnetic parts in the sample.

The reported interaction constants vary in the literature, depending on the technique used. According to one publication for $Sr_3Cr_2O_8$ the interaction constants are $J_0 = 5.55\,\text{meV} \mathrel{\widehat{=}} 64.4\,\text{K}$ and $J' = 3.6\,\text{meV} \mathrel{\widehat{=}} 42\,\text{K}$ according to inelastic neutron scattering, and $J_0 = 5.51\,\text{meV} \mathrel{\widehat{=}} 63.9\,\text{K}$ and J' somewhere between $1.2\,\text{meV} \mathrel{\widehat{=}} 14\,\text{K}$ and $2.0\,\text{meV} \mathrel{\widehat{=}} 23\,\text{K}$ according to susceptibility measurements [63]. According to another study, the values are $J_0/k_B = 62.0(1)\,\text{K}$ and $J'/k_B = 6(2)\,\text{K}$ [64].

Depending on the measurement method, the values for J' can vary quite dramatically. Small variations can also be found for the values of g. For $Sr_3Cr_2O_8$, we use g =1.95 [65].

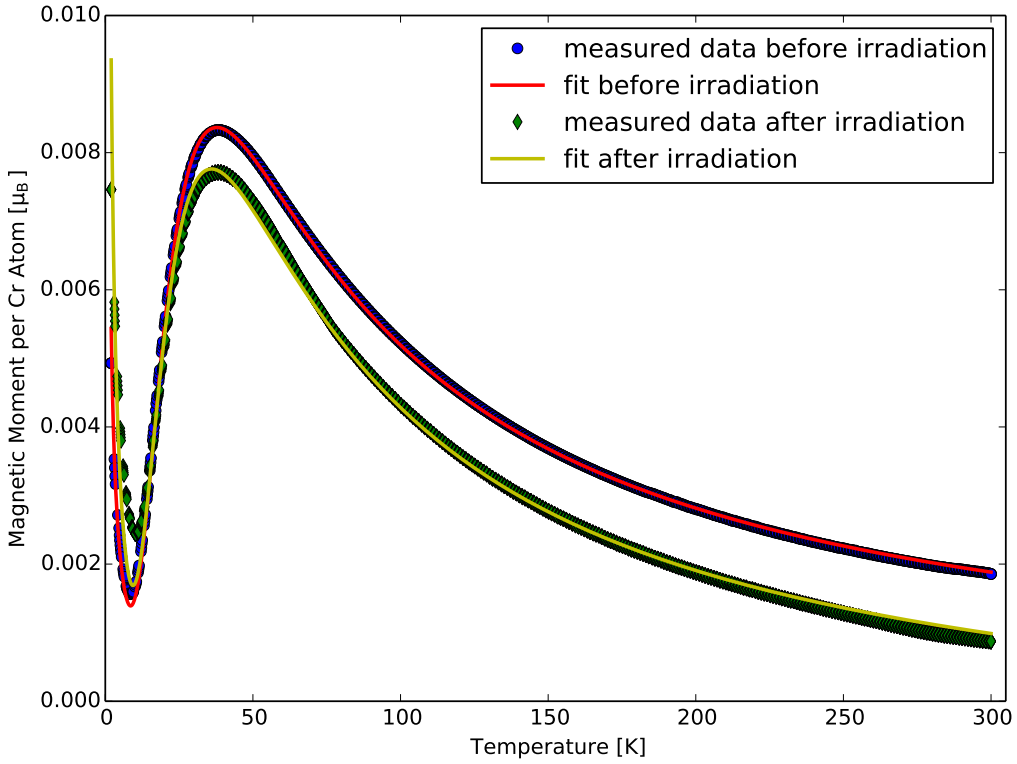

Figure 6.12: The the $m(T)$ measurement of $Sr_3Cr_2O_8$ for a field of 1 T *before and after neutron irradiation for* 4 min.

The measurements before and after the 4 min irradiation are shown in figure 6.12, together with the corresponding fits according to equation 4.6, with an additional constant background, which is very small. For the measurement before the irradiation the fit is in reasonable agreement with the data. This is in contrast to the measurement after the irradiation, where the fit does not agree with the data as well.

A closer look at lower temperatures is taken in figure 6.13. Here, the deviation of the fit from the measured data after the irradiation can be clearly seen. The resulting parameters from these fits are given in table 6.4. Due to the bad fit, the values describing the curve after the irradiation should be looked at with reservation.

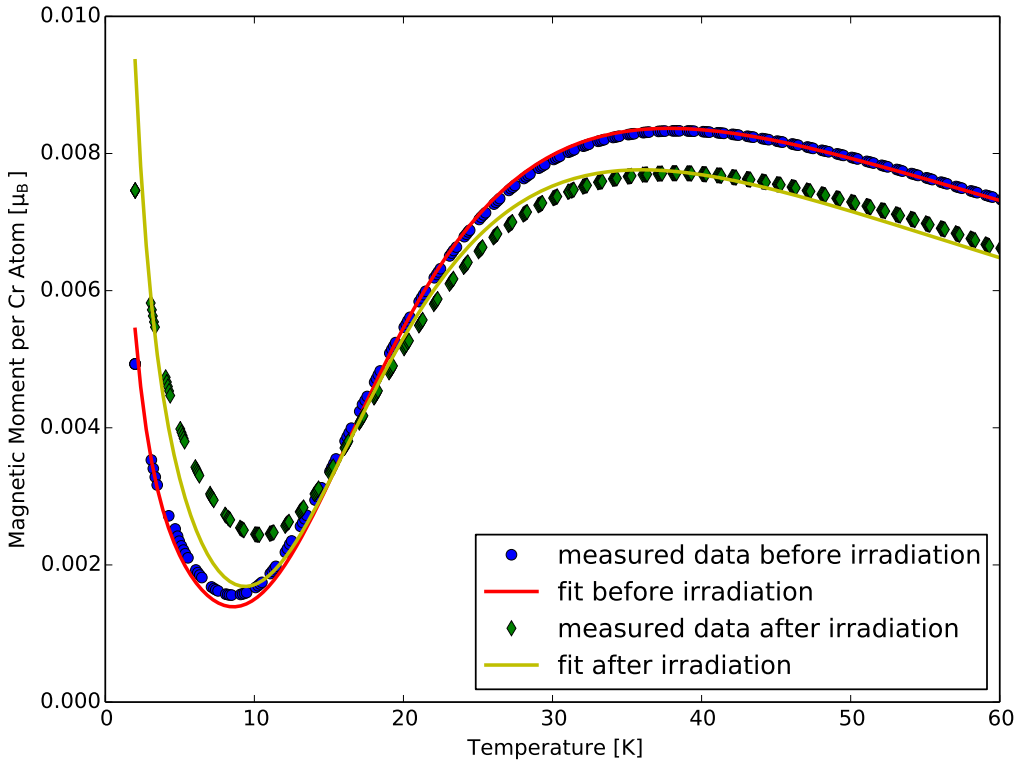

Figure 6.13: A zoomed version of figure 6.12.

The increase in the number of paramagnetic, i.e. un-dimerized, Cr atoms N_p increases, and the number of dimerized atoms N_d decreases. This is in agreement with the simple picture of the destruction of dimers.

In figure 6.14 we show the $m(T)$ data for the 30 min irradiation. The corresponding parameters of the fits are given in table 6.5. The number of paramagnetic atoms increases again and the that of the dimerized atoms decreases. However, the difference in the numbers before and after are smaller than in the irradiation for 4 min. We would have expected the number of destroyed dimers and created paramagnets to depend approximately linearly on the irradiation time. We do not have an explanation for this behaviour yet. Considering that 30 min was the longest irradiation time and the induced damages are fairly small, a longer irradiation time should probably be taken in future experiments. It also needs to be noted that the ratio of paramagnetic atoms to dimerized atoms before the irradiation is larger in this sample than in the sample used in the 4 min irradiation. This could have an effect on the accuracy of the fit since the magnetic moment of a paramagnetic atom is much larger than that of a dimerized atom.

quantity	before	after
N_p	$5.18(2) \times 10^{17}$	$9.52(6) \times 10^{17}$
N_d	$2.87(1) \times 10^{19}$	$2.72(1) \times 10^{19}$
J_0/k_B	$62.07(4)\,\mathrm{K}$	$60.2(1)\,\mathrm{K}$
J'/k_B	$4(1)\,\mathrm{K}$	$0.0(5)\,\mathrm{K}$

Table 6.4: The values of the fitted functions for $Sr_3Cr_3O_8$ before and after neutron irradiation for 4 min.

quantity	before	after
N_p	$3.040(6) \times 10^{18}$	$3.349(7) \times 10^{18}$
N_d	$6.22(3) \times 10^{19}$	$5.87(1) \times 10^{19}$
J_0/k_B	$62.31(4)\,\mathrm{K}$	$61.30(6)\,\mathrm{K}$
J'/k_B	$1.6(13)\,\mathrm{K}$	$0.0(3)\,\mathrm{K}$

Table 6.5: The values of the fitted functions for $Sr_3Cr_2O_8$ before and after neutron irradiation for 30 min.

For $Ba_3Cr_2O_8$ the g-factor is 1.94 [66] and the expected values for the interaction constants are $J_0 = 2.38(2)\,\mathrm{meV} \mathrel{\widehat{=}} 27.6\,\mathrm{K}$ and $J' \leq 0.52(2)\,\mathrm{meV} \mathrel{\widehat{=}} 6.0\,\mathrm{K}$ as measured by inelastic neutron scattering [67]. Values of the fit are shown in table 6.6. A problem we faced with this sample was that it was broken when we received it back after the irradiation. The largest piece was then used for the measurement. The ratio of the masses is $m_\mathrm{before}/m_\mathrm{after} = 1.40$. This is compatible with the numbers in table 6.6 where we have a ratio of 1.53 and 1.42 for N_p and N_d respectively. The only quantity that changes is J', but again, the fit function is not very sensitive to this parameter.

The corresponding plot is shown in figure 6.15. The data after the irradiation are scaled with a factor of 1.4 to adjust for the missing mass. As one can easily see, the two curves are now basically the same. Therefore, we decided not to use $Ba_3Cr_2O_8$ for the irradiation with a total time of 30 min.

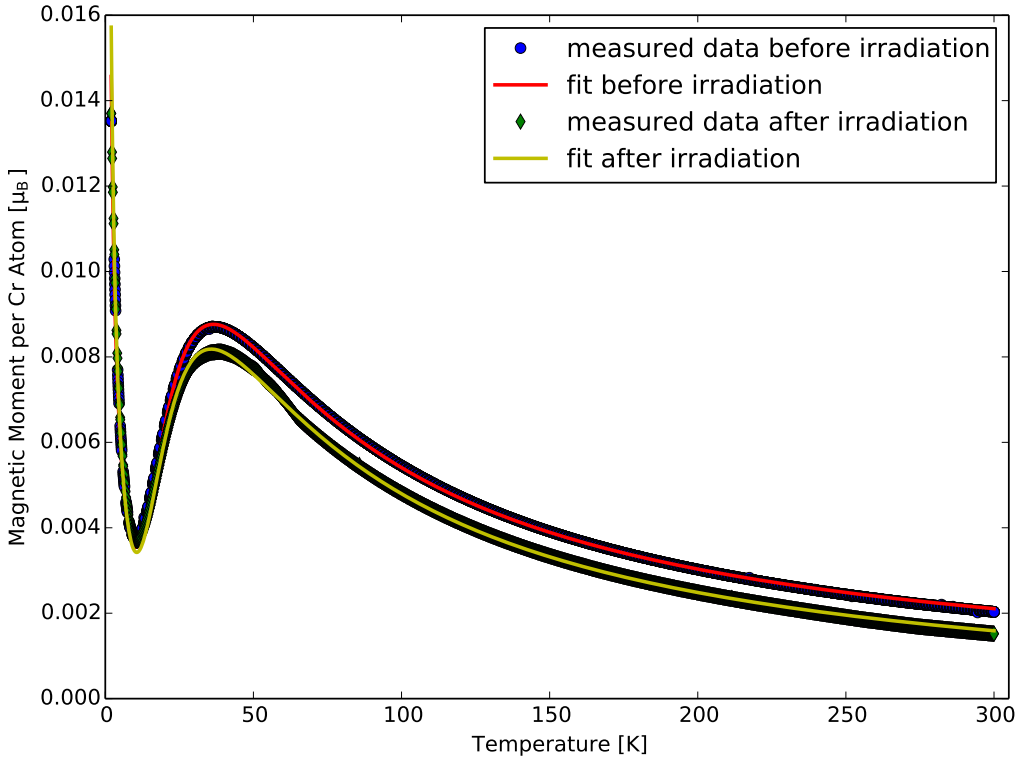

Figure 6.14: The the $m(T)$ measurement for $Sr_3Cr_2O_8$ for a field of 1 T *before and after neutron irradiation for* 30 min.

quantity	before	after
N_p	$2.80(2) \times 10^{18}$	$1.83(1) \times 10^{18}$
N_d	$7.15(6) \times 10^{19}$	$5.03(2) \times 10^{19}$
J_0/k_B	23.66(6) K	24.24(3) K
J'/k_B	20.1(1) K	11.7(6) K

Table 6.6: The values of the fitted functions for $Ba_3Cr_2O_8$ before and after neutron irradiation for 4 min.

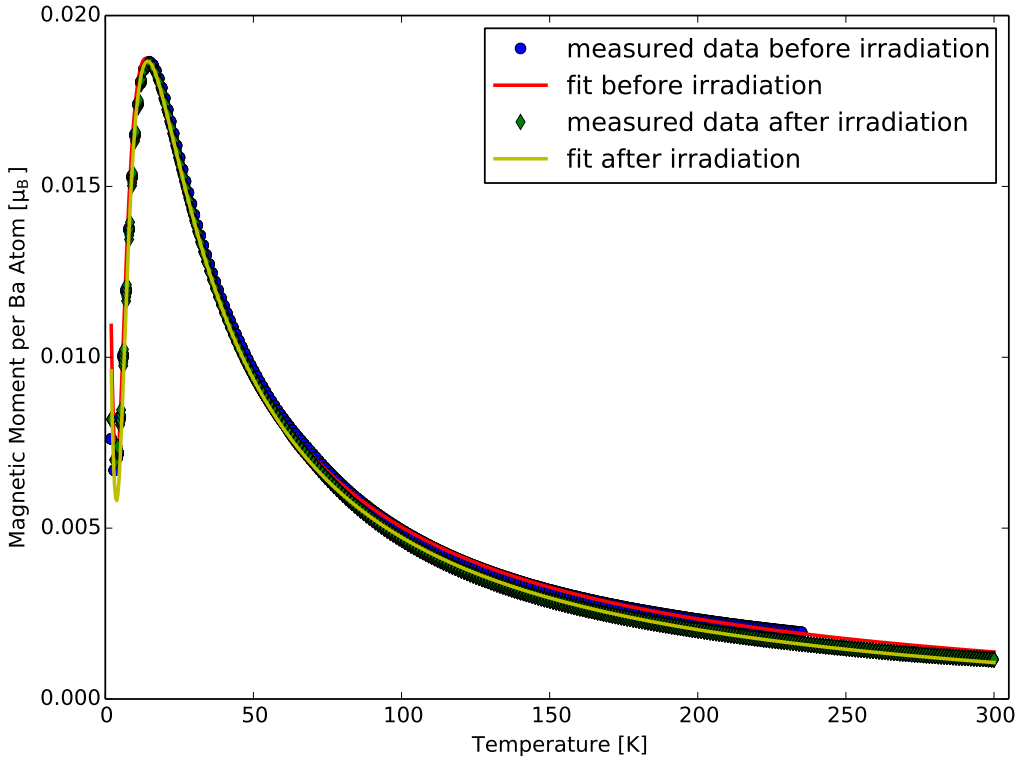

Figure 6.15: The the $m(T)$ measurement for a field of $1\,\mathrm{T}$ before and after neutron irradiation for $4\,\mathrm{min}$ of the $Ba_3Cr_2O_8$ sample. The two curves virtually coincide.

Summary and Outlook

In the first part of this thesis the influence of light irradiation on BSCCO-2223 films was examined. Photoconductivity could be observed with lasers using wavelengths of at least 900 nm. The effect continues to appear for shorter wavelengths at least up to 488 nm, which was the smallest wavelength available using the lasers. Continuous irradiation from a laser diode and pulsed irradiation from a fibre laser do not influence the photoconductivity in a different way. As soon as the laser is turned off, the resistance starts to relax back to the original value on a time scale of one hour. Irradiation at a much shorter wavelength was achieved by using x-rays. These measurements show a time constant much larger than the measurements with visible light, on the order of a day, and a more persistent photoconductivity. Heating the sample above 120 K and subsequent cooling to the temperature of the irradiation reverses the effect, and the resistance is again back at the original value.

Intensity dependent measurements exhibit a behaviour that has not been reported on other materials, by showing an intensity dependence apparently in the form of a threshold, instead of only depending on the total photon dose.

Temperature dependent measurements show that photoconductivity effects are most pronounced at T_c. It also appears that the critical temperature separates temperature regions with different behaviour of the time constant, albeit the measurements are not detailed enough in temperature to make a well founded claim.

The role of defects in the materials, especially oxygen vacancies and oxygen ordering should be investigated further. Nonetheless, this work has already given some insight into the behaviour of a material with different oxygen arrangement than in the most studied YBCO123 system.

In the second part of this thesis the effects of electron and neutron irradiation on magnetic dimer systems were examined. We could show that electrons do not create a significant change in the critical parameters. On the other hand,

neutron irradiation seems to affect the materials under investigation already at relatively low doses. Although the measurements performed to estimate the microscopic conversion of dimers to paramagnetic atoms are inconclusive, the phase diagram changes in a remarkable way. A dose of 1.69×10^{16} thermal neutrons per cm^2 increases the critical temperature by about 0.9 K or decreases the critical field by about 0.4 T. However, it has been observed that in our sample the two methods $m(H)$ and $m(T)$ do not yield the same phase boundary.

To make sure that the shift of the phase boundary is in fact real and not an artefact, the experiments should be repeated and more attention should be paid to the $m(H)$ measurements.

In the long run, microscopic investigations of the structure of the defects using HRTEM, STM or other suitable methods should be made. This would allow for the investigation the defects, their distribution, and their influence on the crystal structure in a direct way, and we could verify that the irradiation does indeed induce point defects as opposed to larger defect structures.

The main goal of these investigations is to be able to tune the critical field in a material in a controlled way, which would be a big step towards the fabrication of conjectured magnetic Josephson junctions [68].

Acknowledgements

Many people contributed to the success of this master's thesis and I am very grateful for their help. In particular I would like to thank the following people:

First I would like to thank Prof. Dr. Andreas Schilling for letting me work in his group and for his guidance and interest in my work.

Dr. Henrik Grundmann was my supervisor for the part on Bose-Einstein condensation. He introduced me to the necessary experimental techniques and guided me throughout my project. His advice and help was always welcome and we have become good friends during our time together.

The part about photoconductivity in superconductors was supervised by Dr. Andreas Engel. His help and experience were very useful for me, for which a thank him very much. I already worked with him during my bachelor's thesis and I was happy to do so again.

Dr. Fabian von Rohr was of great help with his expertise of electrical contacts and his experience with the measurement devices.

Dr. Olaf Bossen and Xiaofu Zhang shared an office with me. I am very grateful for the great atmosphere in the office and also thankful for their help in the lab.

Alsu Gazizulina helped me with the laue diffraction at the PSI, for which I am very grateful to her.

I would also like to thank the rest of the group for their help and interest in my work.

Furthermore I want to thank the many people from the workshop and the electronics workshop. Their expertise was always greatly appreciated and the advice and help we received were of great value for us.

The numerous people working at the PSI should receive my gratitude too, in particular Alex Vögele. He performed the irradiation for us and did the necessary measurements and calculations concerning radioactivity in our samples.

For their help concerning the fabrication of the contacts with the electron-beam evaporator great gratitude goes to the people from Prof. Dr. Fink's group, especially Flavio Wicki and Dr. Conrad Escher.

Bibliography

[1] L. R. Testardi
Destruction of Superconductivity by Laser Light
Phys. Rev. B **4**, 2189 (1971)
http://dx.doi.org/10.1103/PhysRevB.4.2189

[2] J. G. Bednorz, K. A. Müller
Possible high T_c superconductivity in the Ba–La–Cu–O system
Zeitschrift für Physik B Condensed Matter, Volume **64**, Issue 2, pp 189–193 (1986)
http://dx.doi.org/10.1007/BF01303701

[3] A. Schilling, M. Cantoni, J. D. Guo, H. R. Ott
Superconductivity above 130 K in the Hg–Ba–Ca–Cu–O system
Nature **363**, 56-58 (1993)
http://dx.doi.org/10.1038/363056a0

[4] V. I. Kudinov, I. L. Chaplygin, A. I. Kirilyuk, N. M. Kreines, R. Laiho, E. Lähderanta, and C. Ayache
Persistent photoconductivity in $YBa_2Cu_3O_{6+x}$ films as a method of photodoping toward metallic and superconducting phases
Phys. Rev. B **47**, 9017 (1993)
http://dx.doi.org/10.1103/PhysRevB.47.9017

[5] Z. M. Zhang, A. Frenkel
Thermal and nonequilibrium responses of superconductors for radiation detectors
Journal of Superconductivity, Volume 7, Issue 6, pp 871-884 (1994)
http://dx.doi.org/10.1007/BF00732263

[6] G. N. Gol'tsman, O. Okunev, G. Chulkova, A. Lipatov, A. Semenov, K. Smirnov, B. Voronov, A. Dzardanov, C. Williams, Roman Sobolewski
Picosecond superconducting single-photon optical detector

Appl. Phys. Lett. 79, 705 (2001)
http://link.aip.org/link/doi/10.1063/1.1388868

[7] David Lederman, J. Hasen, Ivan K. Schuller, E. Osquiguil and Y. Bruynseraede
Photoinduced superconductivity and structural changes in high temperature superconducting films
Appl. Phys. Lett. **64**, 652 (1994)
http://dx.doi.org/10.1063/1.111078

[8] L. Shi, G. L. Huang, C. Lehane, J. P. Zheng and H. S. Kwok
Generation and measurement of picosecond voltage pulses in $YBa_2Cu_3O_7$ thin films
Appl. Phys. Lett. **61**, 489 (1992)
http://dx.doi.org/10.1063/1.107866

[9] Kirilyuk A. I., Kreines N. M., Kudinov V. I.
Frozen photoconductivity in YBaCuO films
JETP Letters, Volume 52, Issue 1, page 49 (1990)
http://www.jetpletters.ac.ru/ps/1152/article_17435.pdf

[10] G. Nieva, E. Osquiguil, J. Guimpel, M. Maenhoudt, B. Wuyts, Y. Bruynseraede, M. B. Maple and Ivan K. Schuller
Photoinduced enhancement of superconductivity
Appl. Phys. Lett. **60**, 2159 (1992)
http://dx.doi.org/10.1063/1.107069

[11] G. Nieva, E. Osquiguil, J. Guimpel, M. Maenhoudt, B. Wuyts, Y. Bruynseraede, M. B. Maple, and Ivan K. Schuller
Photoinduced changes in the transport properties of oxygen-deficient $YBa_2Cu_3O_x$
Phys. Rev. **B** 46, 14249 (1992)
http://dx.doi.org/10.1103/PhysRevB.46.14249

[12] V. M. Dmitriev, V. V. Eremenko, I. S. Kachur, E. V. Khristenko, V. G. Piryatinskaya, O. R. Prikhod'ko, V. V. Shapiro
Photo-illumination effect on critical current of $YBa_2Cu_3O_{6+x}$ films
Physica C Volumes 235–240, Part 5, Pages 3015–3016 (1994)
http://dx.doi.org/10.1016/0921-4534(94)91034-0

[13] A. Hoffmann, Ivan K. Schuller, Z. F. Ren, J. Y. Lao, and J. H. Wang
Persistent photoconductivity in overdoped high-T_c thin films

Phys. Rev. B **56**, 13742 (1997)
http://dx.doi.org/10.1103/PhysRevB.56.13742

[14] Hiroshi Maeda, Yoshiaki Tanaka, Masao Fukutomi, Toshihisa Asano
A New High-T_c Oxide Superconductor without a Rare Earth Element
Jpn. J. Appl. Phys. **27** L209 (1988)
http://dx.doi.org/10.1143/JJAP.27.L209

[15] J. L. Tallon, R. G. Buckley, P. W. Gilberd, M. R. Presland, I. W. M. Brown, M. E. Bowden, L. A. Christian & R. Goguel
High-T_c superconducting phases in the series $Bi_{2.1}(Ca,Sr)_{n+l}Cu_nO_{2n+4+\delta}$
Nature **333**, 153 - 156 (1988)
http://dx.doi.org/10.1038/333153a0

[16] A. Gilabert, A. Hoffmann, M. G. Medici, I. K. Schuller
Photodoping Effects in High Critical Temperature Superconducting Films and Josephson Junctions
Journal of Superconductivity, Volume **13**, Issue 1, pp 1-20 (2000)
http://dx.doi.org/10.1023/A:1007761805713

[17] B. W. Veal, H. You, A. P. Paulikas, H. Shi, Y. Fang, and J. W. Downey
Time-dependent superconducting behavior of oxygen-deficient $YBa_2Cu_3O_x$: Possible annealing of oxygen vacancies at 300 K
Phys. Rev. B **42**, 4770 (1990)
http://dx.doi.org/10.1103/PhysRevB.42.4770

[18] T. Endo, A. Hoffmann, J. Santamaria, and Ivan K. Schuller
Enhancement of persistent photoconductivity by uv excitation in $GdBa_2Cu_3O_{6.3}$
Phys. Rev. B **54**, R3750(R) (1996)
http://dx.doi.org/10.1103/PhysRevB.54.R3750

[19] I. P. Krylov
Mechanism for the frozen photoconductivity of $YBa_2Cu_3O_{7-\delta}$
JETP Lett. **52**, 442 (1990)
http://www.jetpletters.ac.ru/ps/1159/article_17533.shtml

[20] M. Jiménez de Castro and J. L. Alvarez Rivas
X-ray-induced photoconductivity in $YBa_2Cu_3O_6$ between 70 and 300 K
Phys. Rev. B **53**, 8614 (1996)
http://dx.doi.org/10.1103/PhysRevB.53.8614

[21] E. Osquiguil, M. Maenhoudt, B. Wuyts, Y. Bruynseraede, D. Lederman, and Ivan K. Schuller
Photoexcitation and oxygen ordering in $YBa_2Cu_3O_x$ films
Phys. Rev. B **49**, 3675(R) (1994)
http://dx.doi.org/10.1103/PhysRevB.49.3675

[22] A Matsumoto, H Kitaguchi
Critical current density enhancement of Bi, Pb-2223 thin film fabricated by RF sputtering and post-annealing processes
Supercond. Sci. Technol. **27** 015002 (2014)
http://dx.doi.org/10.1088/0953-2048/27/1/015002

[23] Jerome Faist, Federico Capasso, Deborah L. Sivco, Carlo Sirtori, Albert L. Hutchinson, and Alfred Y. Cho
Quantum Cascade Laser
Science **264**, 553 (1994)
http://dx.doi.org/10.1126/science.264.5158.553

[24] Michalis N. Zervas, Christophe A. Codemard
High Power Fiber Lasers: A Review
IEEE Journal of Selected Topics in Quantum Electronics, Volume 20, Issue 5, 0904123 (2014)
http://dx.doi.org/10.1109/JSTQE.2014.2321279

[25] John M. Dudley, Goëry Genty, Stéphane Coen
Supercontinuum generation in photonic crystal fiber
Rev. Mod. Phys. 78, 1135 (2006)
http://dx.doi.org/10.1103/RevModPhys.78.1135

[26] RP Photonics Encyclopedia
Supercontinuum Generation
http://www.rp-photonics.com/supercontinuum_generation.html

[27] S. E. Harris, R. W. Wallace
Acousto-Optic Tunable Filter
J. Opt. Soc. Am. **59**, 744-747 (1969)
http://dx.doi.org/10.1364/JOSA.59.000744

[28] S. E. Harris, S. T. K. Nieh, R. S. Feigelson
$CaMoO_4$ electronically tunable optical filter
Appl. Phys. Lett. **17**, 223 (1970)
http://dx.doi.org/10.1063/1.1653374

[29] Thomas J. Fellers, Michael W. Davidson; Olympus Corporation
Acousto-Optic Tunable Filters (AOTFs)
http://www.olympusfluoview.com/theory/aotfintro.html

[30] W Markowitsch, W Lang, J D Pedarnig and D Bäuerle
Persistent photoconductivity in oxygen-deficient and ion-irradiated $YBa_2Cu_3O_x$
Supercond. Sci. Technol. **22** 034011 (2009)
http://dx.doi.org/10.1088/0953-2048/22/3/034011

[31] S. L. Bud'ko, H. H. Feng, M. F. Davis, J. C. Wolfe, and P. H. Hor
Persistent photoconductivity in insulating and superconducting YBa2Cu3Ox thin films: Temperature and spectral dependence
Phys. Rev. B **48**, 16707 (1993)
http://dx.doi.org/10.1103/PhysRevB.48.16707

[32] Center for X-Ray Optics, Lawrence Berkeley National Laboratory
X-Ray Attenuation Length
http://henke.lbl.gov/optical_constants/atten2.html

[33] P. Kapitza
Viscosity of Liquid Helium below the λ-Point
Nature **141**, 74 (1938)
http://dx.doi.org/10.1038/141074a0

[34] J. F. Allen, A. D. Misener
Flow of Liquid Helium II
Nature **141**, 75 (1938)
http://dx.doi.org/10.1038/141075a0

[35] M. H. Anderson, J. R. Ensher, M. R. Matthews, C. E. Wieman, E. A. Cornell
Observation of Bose-Einstein Condensation in a Dilute Atomic Vapor
Science Vol. **269** no. 5221 pp. 198-201 (1995)
http://dx.doi.org/10.1126/science.269.5221.198

[36] K. B. Davis, M.-O. Mewes, M. R. Andrews, N. J. van Druten, D. S. Durfee, D. M. Kurn, and W. Ketterle
Bose-Einstein Condensation in a Gas of Sodium Atoms
Phys. Rev. Lett. **75**, 3969 (1995)
http://dx.doi.org/10.1103/PhysRevLett.75.3969

[37] A. Oosawa, M. Ishii and H. Tanaka
Field-induced three-dimensional magnetic ordering in the spin-gap system $TlCuCl_3$
J. Phys.: Condens. Matter **11** 265 (1999)
http://dx.doi.org/10.1088/0953-8984/11/1/021

[38] T. Nikuni, M. Oshikawa, A. Oosawa, H. Tanaka
Bose-Einstein Condensation of Dilute Magnons in $TlCuCl_3$
Phys. Rev. Lett. **84**, 5868 (2000)
http://dx.doi.org/10.1103/PhysRevLett.84.5868

[39] Thierry Giamarchi, Christian Rüegg, Oleg Tchernyshyov
Bose–Einstein condensation in magnetic insulators
Nature Physics **4**, 198 - 204 (2008)
http://dx.doi.org/10.1038/nphys893

[40] M B Stone, C Broholm, D H Reich, P Schiffer, O Tchernyshyov, P Vorderwisch and N Harrison
Field-driven phase transitions in a quasi-two-dimensional quantum antiferromagnet
New J. Phys. **9** 31 (2007)
http://dx.doi.org/10.1088/1367-2630/9/2/031

[41] T. Saha-Dasgupta and R. Valentí
Comparative study between two quantum spin systems $KCuCl_3$ and $TlCuCl_3$
Europhys. Lett. **60** 309 (2002)
http://dx.doi.org/10.1209/epl/i2002-00351-x

[42] Akira Oosawa and Hidekazu Tanaka
Random bond effect in the quantum spin system $(Tl_{1-x}K_x)CuCl_3$
Phys. Rev. B **65**, 184437 (2002)
http://dx.doi.org/10.1103/PhysRevB.65.184437

[43] Fumiko Yamada, Hidekazu Tanaka, Toshio Ono, and Hiroyuki Nojiri
Transition from Bose glass to a condensate of triplons in $Tl_{1-x}K_xCuCl_3$
Phys. Rev. B **83**, 020409(R) (2011)
http://dx.doi.org/10.1103/PhysRevB.83.020409

[44] Masashi Fujisawa, Toshio Ono, Hideyasu Fujiwara, Hidekazu Tanaka, Vadim Sikolenko, Michael Meissner, Peter Smeibidl, Sebastian Gerischer, and Hans A. Graf

Drastic Change of Magnetic Phase Diagram in Doped Quantum Antiferromagnet $TlCu_{1-x}Mg_xCl_3$
J. Phys. Soc. Jpn. **75**, 033702 (2006)
http://dx.doi.org/10.1143/JPSJ.75.033702

[45] Abdulla Rakhimov, Shuhrat Mardonov, E Ya Sherman and Andreas Schilling
The effects of disorder in dimerized quantum magnets in mean field approximations
New J. Phys. **14** 113010 (2012)
http://dx.doi.org/10.1088/1367-2630/14/11/113010

[46] Ch. Rüegg, N. Cavadini, A. Furrer, H.-U. Güdel, K. Krämer, H. Mutka, A. Wildes, K. Habicht, P. Vorderwisch
Bose–Einstein condensation of the triplet states in the magnetic insulator $TlCuCl_3$ Nature **423**, 62-65 (2003)
http://dx.doi.org/10.1038/nature01617

[47] V. N. Glazkov, A. I. Smirnov, H. Tanaka, and A. Oosawa
Spin-resonance modes of the spin-gap magnet $TlCuCl_3$
Phys. Rev. B **69**, 184410 (2004)
http://dx.doi.org/10.1103/PhysRevB.69.184410

[48] T Fujiwara, H Inoue, A Oosawa, R Tsunoda, T Goto, T Suzuki, Y Shindo, H Tanaka, T Sasaki, N Kobayashi, S Awaji and K Watanabe
Cu-NMR study on the disordered quantum spin magnet with the Bose-glass ground state
J. Phys.: Conf. Ser. **51** 199 (2006)
http://dx.doi.org/10.1088/1742-6596/51/1/046

[49] A. Oosawa, H. Aruga Katori, and H. Tanaka
Specific heat study of the field-induced magnetic ordering in the spin-gap system $TlCuCl_3$
Phys. Rev. B **63**, 134416 (2001)
http://dx.doi.org/10.1103/PhysRevB.63.134416

[50] E. Ya. Sherman, P. Lemmens, B. Busse, A. Oosawa, and H. Tanaka
Sound Attenuation Study on the Bose-Einstein Condensation of Magnons in $TlCuCl_3$
Phys. Rev. Lett. **91**, 057201 (2003)
http://dx.doi.org/10.1103/PhysRevLett.91.057201

[51] Kazutaka Kudo, Mitsuhiro Yamazaki, Takayuki Kawamata, Takashi Noji, Yoji Koike, Terukazu Nishizaki, Norio Kobayashi, and Hidekazu Tanaka
Drastic Enhancement of Thermal Conductivity in the Bose–Einstein Condensed State of $TlCuCl_3$
J. Phys. Soc. Jpn. **73**, 2358 (2004)
http://dx.doi.org/10.1143/JPSJ.73.2358

[52] NIST National Institute of Standards and Technology, ESTAR database
http://physics.nist.gov/PhysRefData/Star/Text/method.html

[53] Markus Schmitt
Optimierung dynamischer elektrischer Eigenschaften von Kompensationsbauelementen
Ph.D. thesis, Technische Universität München (2004)
http://www.tep.e-technik.tu-muenchen.de/media/Dissertationen/DISS_schmitt.pdf

[54] Hj. Mattausch and Hk. Müller-Buschbaum
Zur Kristallstruktur von $Ba_2(CrO_4)_2$
Z. Naturforsch. **27 b**, 739 (1972)
http://zfn.mpdl.mpg.de/data/Reihe_B/27/ZNB-1972-27b-0739.pdf

[55] E. Cuno and Hk. Müller-Buschbaum
Ein Beitrag zur Kristallchemie der Erdalkalimetall-Oxochromate(V): $Sr_3(CrO_4)_2$ und $Sr_{18}Ca_3Cr_{14}O_{56}$
Z. anorg. allg. Chem. **572**, 95 (1989)
http://dx.doi.org/10.1002/zaac.19895720111

[56] John Clarke
SQUIDs
Scientific American **271**, 46 (1994)
http://dx.doi.org/10.1038/scientificamerican0894-46

[57] M Sawicki, W Stefanowicz and A Ney
Sensitive SQUID magnetometry for studying nanomagnetism
Semicond. Sci. Technol. **26** 064006 (2011)
http://dx.doi.org/10.1088/0268-1242/26/6/064006

[58] Paul Scherrer Institut, Neutron Irradiation Service
http://www.psi.ch/nis/parameters

[59] Paul Scherrer Institut, SINQ
http://www.psi.ch/bsq/sinq-facility

[60] C. A. M. van der Klein, P. H. Kes, H. van Beelen, D. de Klerk
The effect of neutron irradiation damage on the magnetic behavior of superconducting niobium in stationary fields
Journal of Low Temperature Physics, Volume **16**, 169 (1974)
http://dx.doi.org/10.1007/BF00655866

[61] J. R. de Laeter, J. K. Böhlke, P. De Bièvre, H. Hidaka, H. S. Peiser, K. J. R. Rosman and P. D. P. Taylor
Atomic weights of the elements. Review 2000 (IUPAC Technical Report)
Pure Appl. Chem., Vol. **75**, No. 6, p. 683 (2003)
http://dx.doi.org/10.1351/pac200375060683

[62] Nuclear Data Section, International Atomic Energy Agency
NGATLAS Atlas of Neutron Capture Cross Sections
https://www-nds.iaea.org/ngatlas2/

[63] D. L. Quintero-Castro, B. Lake, E. M. Wheeler, A. T. M. N. Islam, T. Guidi, K. C. Rule, Z. Izaola, M. Russina, K. Kiefer, and Y. Skourski
Magnetic excitations of the gapped quantum spin dimer antiferromagnet $Sr_3Cr_2O_8$
Phys. Rev. B **81**, 014415 (2010)
http://dx.doi.org/10.1103/PhysRevB.81.014415

[64] Yogesh Singh and D. C. Johnston
Singlet ground state in the spin-$\frac{1}{2}$ *dimer compound* $Sr_3Cr_2O_8$
Phys. Rev. B **76**, 012407 (2007)
http://dx.doi.org/10.1103/PhysRevB.76.012407

[65] H. Grundmann
Tuning the Bose-Einstein Condensation in Spin Dimer Quantum Magnets
Ph.D. Thesis, University of Zurich (2014)

[66] Zhe Wang, D. Kamenskyi, O. Cépas, M. Schmidt, D. L. Quintero-Castro, A. T. M. N. Islam, B. Lake, A. A. Aczel, H. A. Dabkowska, A. B. Dabkowski, G. M. Luke, Yuan Wan, A. Loidl, M. Ozerov, J. Wosnitza, S. A. Zvyagin, and J. Deisenhofer
High-field electron spin resonance spectroscopy of singlet-triplet transitions in the spin-dimer systems $Sr_3Cr_2O_8$ *and* $Ba_3Cr_2O_8$

Phys. Rev. B **89**, 174406 (2014)
http://dx.doi.org/10.1103/PhysRevB.89.174406

[67] M. Kofu, J.-H. Kim, S. Ji, S.-H. Lee, H. Ueda, Y. Qiu, H.-J. Kang, M. A. Green, and Y. Ueda
Weakly Coupled s=1/2 Quantum Spin Singlets in $Ba_3Cr_2O_8$
Phys. Rev. Lett. **102**, 037206 (2009)
http://dx.doi.org/10.1103/PhysRevLett.102.037206

[68] Andreas Schilling, Henrik Grundmann
On Josephson effects in insulating spin systems
Annals of Physics, **327**, 2301 (2012)
http://dx.doi.org/10.1016/j.aop.2012.04.004